nature physics

Article

https://doi.org/10.1038/s41567-025-03122-1

Geometry-driven asymmetric cell divisions pattern cell cycles and zygotic genome activation in the zebrafish embryo

Received: 17 May 2025

Accepted: 29 October 2025

Published online: 5 January 2026

Check for updates

Nikhil Mishra, Yuting Irene Li, Edouard Hannezo & Carl-Philipp Heisenberg

Early embryo geometry is one of the most invariant species-specific traits, yet its role in ensuring developmental reproducibility and robustness remains underexplored. Here we show that in zebrafish, the geometry of the fertilized egg—specifically its curvature and volume—serves as a critical initial condition triggering a cascade of events that influence development. The embryo geometry guides patterned asymmetric cell divisions in the blastoderm, generating radial gradients of cell volume and nucleocytoplasmic ratio. These gradients generate mitotic phase waves, with the nucleocytoplasmic ratio determining individual cell cycle periods independently of other cells. We demonstrate that reducing cell autonomy reshapes these waves, emphasizing the instructive role of geometry-derived volume patterns in setting the intrinsic period of the cell cycle oscillator. In addition to organizing cell cycles, early embryo geometry spatially patterns zygotic genome activation at the midblastula transition, a key step in establishing embryonic autonomy. Disrupting the embryo shape alters the zygotic genome activation pattern and causes ectopic germ layer specification, underscoring the developmental significance of geometry. Together, our findings reveal a symmetry-breaking function of early embryo geometry in coordinating cell cycle and transcriptional patterning.

Developmental reproducibility and robustness are critical for the survival of a species. Understanding the foundations of this robustness is, therefore, a question of fundamental importance and has become a central focus of research. Although most studies have concentrated on the genetic and molecular mechanisms underlying development, the potential influence of geometry on developmental robustness has remained largely overlooked.

Recent work using minimal active matter models has revealed that geometry and curvature play a pivotal role in the mechanical response of epithelial sheets[1–5]. These insights can, for example, account for the anisotropic distribution of myosin II observed in *Drosophila* embryos[6]. Such findings highlight geometry as a key organizer of mechanical force generation during morphogenesis. Yet, whether—and how—geometry governs more complex, large-scale developmental processes, such as embryo patterning and coordinated cell divisions, remains an open question.

Metazoan development begins with a single cell, the zygote, which undergoes several rounds of rapid divisions (cleavages) to generate a large population of cells capable of adopting multiple fates and exhibiting diverse morphogenetic behaviours. In many species, these early divisions are initially highly synchronous. This cell cycle synchrony is best understood in *Drosophila*, where it is driven by the propagation of a chemical wave. In cleavage-stage *Drosophila* embryos, which are syncytial, nuclear cycles synchronize through 'sweep waves'—coupling-independent phase waves emerging on top of gradients of cyclin-dependent kinase 1 (Cdk1) activity established

Institute of Science and Technology Austria, Klosterneuburg, Austria. e-mail: heisenberg@ista.ac.at

through reaction–diffusion dynamics[7,8]. Similar mechanisms have been observed in *Xenopus* egg extracts, another syncytial system, where nuclear divisions are coordinated by trigger waves of Cdk1 activity[9]. By contrast, in intact *Xenopus* embryos, where cells are fully separated, early cleavage divisions synchronize independently of cell–cell coupling[10]. Importantly, across systems, the propagation of cell cycle waves slows progressively with successive division rounds, leading to 'metasynchronization', where cell cycles remain spatially patterned before eventually becoming fully desynchronized[7,10,11].

Cell cycles in the zebrafish embryo are synchronized in a cell-autonomous manner

Initial cleavages in the zebrafish embryo are meroblastic; that is, the cytoplasm but not the yolk is partitioned through cytokinesis[11]. Cell cycles at this stage occur highly synchronously, to begin with, and gradually desynchronize (metasynchrony) before completely desynchronizing at division round 10 (ref. 11). Importantly, although the cleavage-stage cells cycle between only the S and M phases with no detectable gap phases, complete desynchronization around division round 10 is thought to occur mainly due to a heterogeneous introduction of gap phases to the cell cycles[12]. To determine the spatiotemporal pattern of cell divisions in cleavage-stage zebrafish embryos, we recorded time-lapse images of Tg*(actb2:rfp-pcna)* embryos. Due to the absence of gap phases in the cleavage stages, the disappearance of the nuclear red fluorescent protein (RFP)-proliferating cell nuclear antigen (PCNA) localization allowed us to reliably score the conclusion of the S phase and the onset of mitosis[13]. Consistent with previous reports, we observed three distinct phases with different extents of mitotic synchrony[11,14]. In the first three cell division rounds, cell cycles exhibited very high synchrony (synchronous phase) (Fig. 1b and Extended Data Fig. 1a,b). Thereafter, cell divisions from division rounds 4–9 showed slight but clearly detectable delays (metasynchronous phase) (Fig. 1b and Extended Data Fig. 1a,b). These delays increased throughout the metasynchronous phase, with cells in division round 4 dividing with a mean division timing variance of 0.10 min^2 and in division round 9 with 3.43 min^2 (Fig. 1b). In particular, as previously reported, these metasynchronous divisions occurred in a spatiotemporally patterned manner, forming a radial 'mitotic wave' that originates near the animal pole (AP), where cells divide first and propagate towards the margin, where they divide last (Fig. 1c and Extended Data Fig. 1c,d)[11,15,16]. Furthermore, consistent with the increasing variance in division timings during the metasynchronous phase, the speed at which this mitotic wave travels gradually decreased over consecutive division rounds (Fig. 1d). After division round 9, cells divided largely non-synchronously, marking the onset of the asynchronous phase.

To understand how cell cycles are seemingly coordinated into radial mitotic waves during the metasynchronous phase, we asked if their synchronization occurs via cell–cell coupling. To that end, we artificially desynchronized cell cycles at the 32/64-cell stage through mosaic Histone 1 protein injections, previously shown to effectively alter cell cycle progression[17–19]. We found that Histone 1-positive and thus desynchronized cells failed to resynchronize with their neighbouring control cells by division round 9, after which cell cycles normally desynchronize in control embryos (Fig. 1e, Extended Data Fig. 2, Supplementary Section 5 and Supplementary Video2). To address the possibility that these cell cycles could have resynchronized given sufficient time, we assessed the cell cycle progression in embryos ectopically expressing the Cdk1 inhibitor, Chek1, through *chek1* mRNA injection in the one-cell stage embryo, which, by being heterogeneously distributed in the embryo, has previously been shown to interfere with cell cycle synchronization[20]. *chek1*-overexpressing embryos exhibited cell cycle desynchronization considerably earlier than control embryos, and failed to resynchronize despite completing all cleavage division rounds (Fig. 1f, Extended Data Fig. 2and Supplementary Video 3). Collectively, these observations suggest that cell cycle coupling plays only a minor role, if any, in cell cycle synchronization in the zebrafish embryo.

To determine by which coupling-independent mechanism the radial mitotic wave is formed, we analysed the evolution of the mitotic wave through consecutive division rounds. We found that the transition from synchrony to metasynchrony was gradual rather than abrupt, suggesting a progressive accumulation of delays rather than distinct switches leading to the observed loss of synchrony (Fig. 1b). Importantly, this gradual loss of synchrony was due to unequal cell cycle periods. For instance, between the metasynchronous division rounds 6–8, cells at the margin cycled with 2%–4% longer periods than those at the AP (Fig. 1g). This discrepancy arose exclusively due to a longer S phase (assuming absent gap phases), which increased in cells as a function of their distance from the AP (Fig. 1h,i). Although noisy, such period gradients may lead to the observed gradual slowing down of the radial mitotic wave by accumulating increasing delays in the marginal cells over consecutive division rounds. To test this hypothesis, we assumed that the period T is a linear function of the distance z from the AP: $T = T_0\,(1 + \frac{kz}{L})$, where T_0 is the typical period at the AP, L is the total AP–margin distance and k is a dimensionless constant of proportionality. This implies that the speed of the mitotic wave, v, in the nth division round is expected to be inversely proportional to n (Fig. 1d) with $v = \frac{L}{T_0}\frac{1}{kn}$. To compare our experimental observations with these theoretical predictions, we first performed linear regression on the division timings to obtain the wave speed for each division round (Extended Data Fig. 1d). We then fitted the obtained v against $\frac{1}{n}$ using the least squares fit. Using $k = 1.9\%$, we obtained a close match between experiments and theory (Fig. 1d), suggesting that a 1.9% slower cell cycle at the margin would, in principle, be sufficient to explain the observed slowing down of the mitotic waves during consecutive division rounds. Considering that we experimentally observed a 2%–4% longer period at the margin, close to the theoretically predicted 1.9%, this suggests that a linear gradient of cell cycle periods, rather than cell–cell coupling, gives rise to the observed radial mitotic waves found during embryonic cleavages.

We note that constant T and κ are simplifying assumptions, as cell cycle periods increase over rounds and exhibit embryo-to-embryo variations. Incorporating these variations would complicate our analysis due to the difficulty in accurately quantifying the appropriate parameter variations, without altering our qualitative conclusions. Hence, given the reasonable theory–experiment agreement (Fig. 1d) and in the spirit of minimal models, we maintain these assumptions throughout our model analysis, allowing us to focus on the consequences of cell–cell coupling mechanisms.

Increased cell–cell coupling reshapes the mitotic wave and prevents desynchronization

Next, to challenge our conclusion that the mitotic waves are produced in a coupling-independent manner, we asked how they would appear if the cell cycles were instead coupled. To that end, we performed numerical simulations of the Kuramoto model of interacting oscillators on a hemisphere with free boundary conditions[21] (Fig. 2a). The oscillators were placed on a Fibonacci lattice covering the hemisphere, with the nearest neighbours obtained with Delaunay triangulation. The phases of the oscillators obeyed the following equation: $\delta_t\theta_i = \omega_i + \epsilon \sum_j \epsilon N_i \sin(\theta_j - \theta_i)$, where ω_i represents the natural frequency of the ith oscillator, and the second term describes the interactions between neighbouring oscillators parameterized by the interaction strength ϵ, with N_i being the nearest neighbours of the ith oscillator. Due to cell–cell variations, we further assumed the presence of noise in the cell cycle lengths. Mathematically, we decomposed the frequencies into two parts $\omega_i = \varpi(z) + \wedge_i$, where the first term $\varpi(z)$, is the inherent AP–margin oscillation gradient, and the second term is an independent spatial noise with covariance $\langle \wedge_i \wedge_j \rangle = \sigma\delta_{ij}$.

https://doi.org/10.1038/s41567-025-03122-1

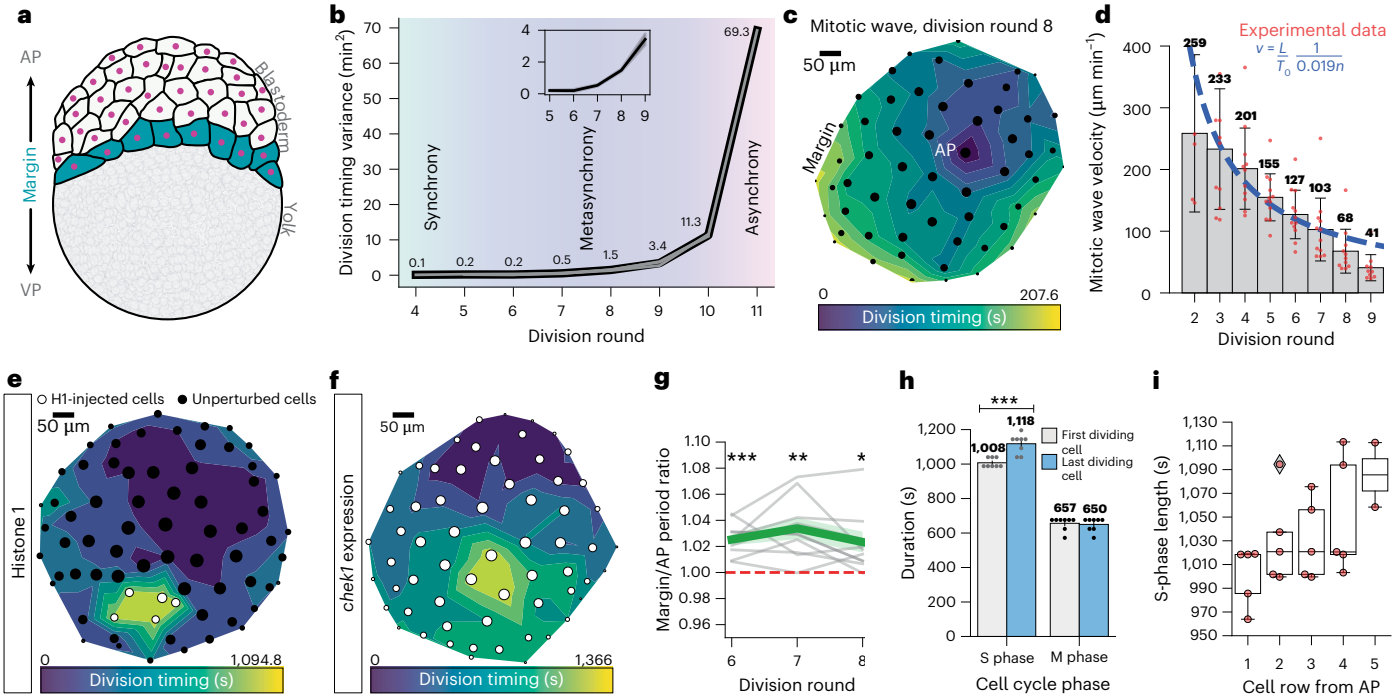

Fig. 1 | Mitotic synchrony gradually decreases as the S phase lengthens along the animal-margin axis. a, Schematic of a zebrafish embryo at the late cleavage stage. The blastoderm is positioned at the AP atop the yolk cell at the vegetal pole (VP). The last row of blastoderm cells (cyan) constitutes the margin. **b**, Line plot of cell division timing variance in Tg(*actb2:rfp-pcna*) embryos for cleavage division rounds 4–11. Grey lines, individual embryos; black line, mean across three embryos. The inset shows variance (mean ± s.e.m.) for division rounds 5–9. **c**, Contour plot of the radial mitotic wave across all surface cells at division round 8 in a representative wild-type embryo. Each dot represents the position of a nucleus along the *x*–*y* plane, and the size of the dot indicates its position along the *z* axis (AP–margin axis). Colours represent the division timing for each nucleus. **d**, Bar plot of mitotic wave velocities (mean ± s.d.), calculated by generating distance–time plots, for cleavage division rounds 2–9, with the red dots showing wave velocities for individual embryos. In sequence from division rounds 2–9, $n = 5, 10, 11, 12, 12, 12, 11$ and 10 embryos, respectively. The blue dashed line indicates the curve described by the equation $v = (L/T_0) \times (1/0.019n)$, where L is the total AP–margin distance, T_0 is the cell cycle period at the AP and n is the division round to represent the effect of a 1.9% period gradient along the AP–margin axis on mitotic wave speeds. **e**,**f**, Representative contour plots of mitotic waves in division round 8 in embryos injected with either 0.3 ng of Histone 1 protein into a single blastomere at the 32-cell stage (**e**) or 12-pg *chek1* mRNA at the 1-cell stage (**f**). **g**, Line plots showing the ratios of cell cycle periods at the margin and AP in division rounds 6–8 in individual embryos (grey lines) and across all embryos (green line, mean ± s.e.m.) for $n = 9$ embryos. Two-tailed one-sample *t*-test. *: 0.0189, **: 0.0033, ***: 0.0004. The red dashed line indicates a ratio of 1, where both marginal and AP cells have the same cell cycle period. **h**, Bar plot of the M-phase and S-phase lengths (mean ± s.e.m.) at division round 8. Dots represent data from individual embryos. Two-tailed Student's *t*-test. $P = 0.0005$, $n = 8$ embryos. **i**, Box plot of S-phase duration in division round 8 as a function of cell position relative to the AP. $n = 5$ embryos. The box in the box plot represents the middle 50% of the distribution, with the line representing the median and the whiskers indicating the minima and maxima.

Specifically, simulations with small interaction strength (ε) and low noise (σ) qualitatively recapitulated the wild-type behaviour, where mitotic waves originated at the AP, and accumulated delays, causing a gradual slowdown over time (Fig. 2b,c). To reach a better quantitative agreement with the data, we considered that the initial cleavage events are incomplete, and consequently, the cytoplasm of early blastomeres remains interconnected through the yolk and via cytoplasmic bridges[22]. These connections are thought to progressively diminish over successive division rounds as cells become smaller—an assumption supported by our observation that single-blastomere injections of 40-kDa dextran, comparable in size to key cell cycle regulators such as Cyclin B1, Cdk1 and Chek1, resulted in its widespread distribution within a single division cycle when performed at the 16-cell stage but not at the 64-cell stage (Extended Data Fig. 4)[22]. On the basis of this, we modelled wild-type embryos as exhibiting a time-dependent coupling that decays to near-zero values, which provided a substantially better fit to the experimental data than models assuming constant, minimal coupling throughout (Supplementary Section 4).

By contrast, the introduction of greater interaction strength and noise led the system to self-organize into smooth mitotic waves originating at the margin, similar to the case in *Xenopus* egg extracts, even though the 'natural' cell cycle lengths at the AP were preset to be shorter on average[23] (Fig. 2b,d). For even larger values of noise, multiple waves emerged from random points of the simulated embryo (Fig. 2b). Overall, this theoretical phase diagram suggests that wild-type embryos are characterized by low-to-intermediate noise and progressively decaying coupling, and that increasing cell coupling should, in theory, shift the origin of the mitotic wave from the AP to the blastoderm margin.

To experimentally test this prediction, we syncytialized cleavage-stage embryos by preventing cytokinesis—but allowing karyokinesis—through transient inactivation of Aurora kinase B[24] (Fig. 2e,f). We reasoned that such a syncytialized embryo would resemble conditions observed in *Drosophila* embryos and *Xenopus* egg extracts—both syncytial systems in which cell cycles are partially or fully synchronized via coupling-dependent trigger waves—and would, therefore, function as a coupled system. Remarkably, consistent with our theoretical predictions, we found that in syncytial embryos, the mitotic wave originated at the margin rather than at the AP, as seen in wild-type embryos (Fig. 2b,d,f and Supplementary Videos 1 and 4). Moreover, by analysing the wave characteristics at division round 8 in syncytial embryos, we were able to estimate the effective ratio of coupling and noise, two competing factors promoting synchronization and desynchronization, respectively (Fig. 2g and Supplementary Section 2).

In particular, our model also predicted key differences in the evolution of cell cycle synchronization—measured by the variance in division timing across division rounds—between wild-type and syncytial

https://doi.org/10.1038/s41567-025-03122-1

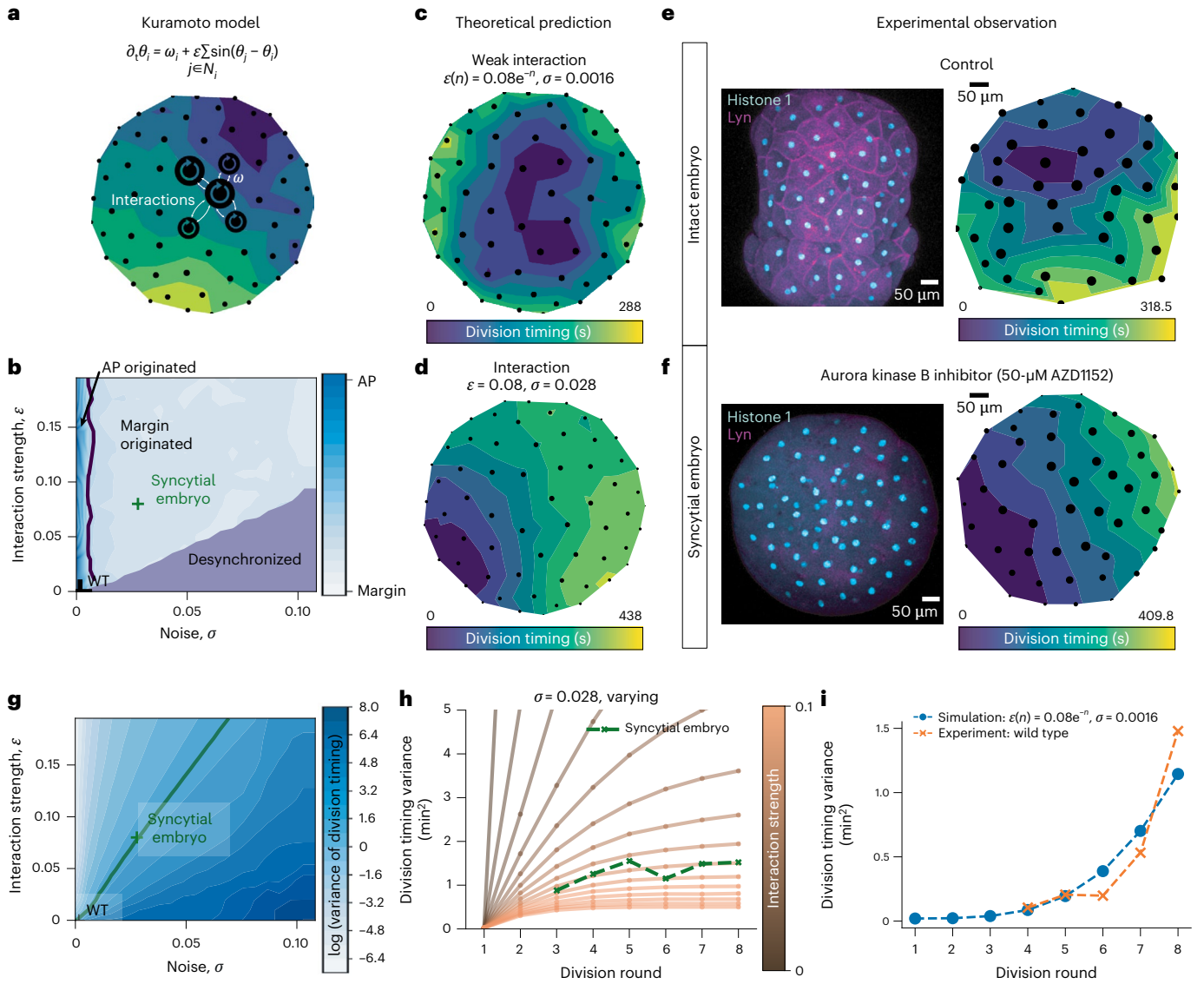

Fig. 2 | Cell–cell coupling repositions the mitotic wave origin to the margin and prevents desynchronization. a, Schematic of our adapted Kuramoto model and the equation describing the evolution of the phase of a cell cycle. In the equation, θ_i represents the cell cycle phase of cell i, and N_i denotes its nearest neighbouring cells, determined through Delaunay triangulation of the hemisphere. The coupling strength ε represents how strongly each cell influences its neighbours' timing. The intrinsic frequency ω_i represents how quickly cell i would progress through its cell cycle in isolation. In the model, each black dot represents a cell positioned on a hemispherical Fibonacci lattice. The dot size increases with height (z) to aid visualization in this top-down projection. Double-headed arrows between dots (shown for one representative cell) indicate coupled neighbours that can influence each other's cell cycle timing. **b**, Phase diagram showing the origin of waves in ε–σ space. The boundary between AP originated and margin originated is thresholded at $z = 0.5$ and the region of desynchronization corresponds to $\langle e^{i\theta_j}\rangle_j < 0.6$, where $\langle\rangle_j$ denotes averaging over all sites. **c**, Contour plot of the radial mitotic wave across all surface cells at division round 8, as predicted using the Kuramoto model of interacting oscillators, assuming an AP–margin period gradient of 1.9% and exponentially decaying cell–cell interaction strength ($\varepsilon = 0.08e^{-n}$, $\sigma = 0.0016$). **d**, Contour plot of the mitotic wave across all surface cells at division round 8, as predicted using the Kuramoto model of interacting oscillators, assuming an AP–margin period gradient of 1.9% and partial interaction between cells ($\varepsilon = 0.08$, $\sigma = 0.028$). **e**, Left: representative image of a 128-cell stage control Tg(*actb2:lyn-tdtomato*) embryo injected with 1 ng of Histone 1-Alexa Fluor 488 at the 1-cell stage to show the presence of a plasma membrane between individual nuclei. Right: contour plot of the radial mitotic wave across all surface cells at division round 8 observed in a control embryo, where nuclear divisions were visualized using either Histone 1-Alexa Fluor 488 injections or using Tg(*actb2:rfp-pcna*) embryos. $n = 7$ embryos. **f**, Left: representative image of a 128-cell stage Tg(*actb2:lyn-tdtomato*) embryo injected with 1 ng of Histone 1-Alexa Fluor 488 at the 1-cell stage and treated with 50 µM of AZD1152 to show the absence of a plasma membrane between the individual nuclei. Right: contour plot of the mitotic wave across all surface cells at division round 8 observed in a representative syncytial embryo, where nuclear divisions were visualized using either Histone 1-Alexa Fluor 488 injections or using Tg(*actb2:rfp-pcna*) embryos. $n = 7$ embryos. **g**, Phase diagram of the Kuramoto model in ε–σ space. The log of the variance of the division timings at division round 8 is plotted. The green solid line indicates the contour line of the observed variance at division round 8 in syncytial embryos. **h**, Variances of division timings for each round for a fixed noise value of $\sigma = 0.028$ as ε varies. The green dashed curve shows the variances measured in syncytial embryos. **i**, Variances of division timings for each round in wild-type embryos (orange) fitted with a curve described by exponentially decaying interaction strength, $\varepsilon(n) = 0.08e^{-n}$, and low noise, $\sigma = 0.0016$ (blue). WT, wild-type.

https://doi.org/10.1038/s41567-025-03122-1

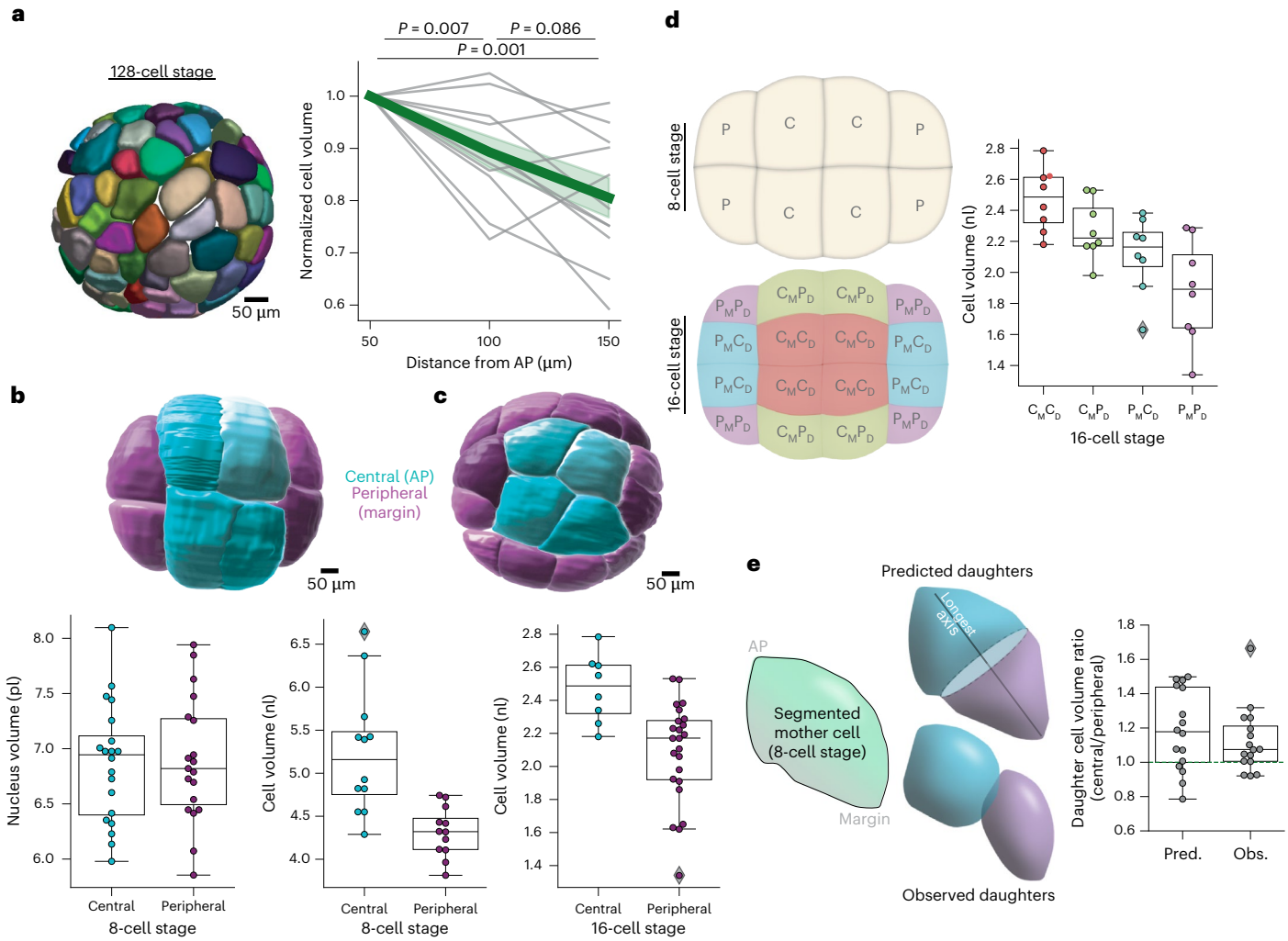

Fig. 3 | Embryo geometry drives asymmetric cell divisions to generate a gradient of cell volumes in the early embryo. a, Representative image of a 128-cell stage embryo (division round 8) with surface cells segmented (left) and line plots showing normalized cell volumes as a function of cell position with respect to the AP (right) in individual embryos. Cell volumes were internally normalized to the average cell volume at the AP in each embryo. $n = 11$ embryos; two-tailed Student's t-test with Benjamini–Hochberg correction for multiple comparisons. **b**, Representative image of an 8-cell stage embryo (division round 4) with surface cells segmented (top) and the box plot showing volumes of individual nuclei and cells based on their position relative to the AP (bottom). Central cells are positioned at the AP, whereas peripheral cells are positioned away from the AP. The box in the box plot represents the middle 50% of the distribution, with the line representing the median and the whiskers indicating the minima and maxima. $n = 20$ central and 19 peripheral nuclei, 5 embryos; 12 central and 12 peripheral cells, 3 embryos. **c**, Representative image of a 16-cell stage embryo (division round 5) with surface cells segmented (top) and the box plot showing volumes of individual cells based on their position relative to the AP. The box in the box plot represents the middle 50% of the distribution, with the line representing the median and the whiskers indicating the minima and maxima. $n = 8$ central and 24 peripheral cells, 2 embryos. **d**, Schematic showing the lineage relationship between cells at the 8-cell stage (top left) and 16-cell stage (bottom left). At the 8-cell stage, cells marked 'C' are centrally positioned, and those marked 'P' are peripherally positioned. At the 16-cell stage, cells are labelled to indicate both their positions (C_D, centrally; P_D, peripherally) and the identities of their mother cells (C_M, centrally positioned mother cell; P_M, peripherally positioned mother cell). Box plot showing the distribution of cell volumes at the 16-cell stage based on each cell's position and lineage identity (right). The box in the box plot represents the middle 50% of the distribution, with the line representing the median and the whiskers indicating the minima and maxima. $n = 8$ cells for each category, 2 embryos. **e**, Schematic showing the pipeline for predicting daughter cell volumes at the 16-cell stage (left). Each segmented cell surface from the 8-cell stage was used to identify the longest cell axis, which was then bisected to obtain daughter cells at the 16-cell stage. Box plot showing a comparison between the ratios of volumes of the central and peripheral daughter cells obtained from each cell division, respectively, either predicted (Pred.) or experimentally observed (Obs.). The box in the box plot represents the middle 50% of the distribution, with the line representing the median and the whiskers indicating the minima and maxima (right). $n = 16$ cell pairs, 2 embryos.

embryos: in the absence of coupling (wild-type embryos), noise is expected to accumulate progressively, resulting in a monotonically increasing variance in division timing. By contrast, in the presence of coupling (syncytial embryos), this variance should plateau over time, with a characteristic timescale determined by the coupling strength (Fig. 2h). Strikingly, our experimental observations confirmed this prediction. In syncytial embryos—unlike in wild-types—'cells' continued to cycle metasynchronously even beyond division round 10, indicating a strong coupling between cell cycles (Extended Data Fig. 3a and Supplementary Videos 1 and 4). The temporal evolution of variance closely matched our theoretical prediction, particularly for $\varepsilon = 0.08$ and $\sigma = 0.028$ (Fig. 2h and Supplementary Section 2). By contrast, wild-type embryos exhibited continuously increasing variance, which could be quantitatively explained by the incomplete nature of cytokinesis during early cleavages, suggesting the presence of a transient coupling that rapidly diminishes as development progresses.

Finally, to further challenge the notion of the increased coupling of cells in syncytial embryos, we injected *chek1* mRNA into embryos before syncytialization and assessed whether they could resist premature desynchronization typically observed when *chek1* was overexpressed in wild-type embryos (Fig. 1f, Extended Data Fig. 1 and Supplementary Video 3). We theoretically reasoned that the coupling inferred for syncytial embryos is large enough that it can override a substantial increase in noise, such as the desynchronizing effects of *chek1* expression (Fig. 2b). Indeed, we found that in *chek1*-overexpressing embryos, the mitotic waves originated at the margin and cells continued to cycle metasynchronously even beyond division round 10, suggesting that cells in the syncytial embryo are, in fact, tightly coupled (Extended Data Fig. 3b,c and Supplementary Video 5). By extension, this implies that such a coupling is absent/minimal in wild-type embryos and, consequently, that mitotic waves are produced largely independently of cell–cell interactions in wild-type embryos. Collectively, these findings suggest that cell cycles are only weakly coupled during cleavages and that metasynchrony arises predominantly by cell-autonomous processes.

Early embryo geometry establishes a cell volume gradient along the AP–margin axis through guided asymmetric cell divisions

For the cell cycle to slowdown from the AP to the margin in a predominantly cell-autonomous manner, there must be a factor causing an unequal lengthening of the S phase along the AP–margin axis. Among the most important factors regulating the S-phase length is the nucleocytoplasmic (N/C) ratio[25,26]. A high N/C ratio causes S-phase lengthening, for instance, by retarding Cdk1 activation[25]. Consistent with such an effect of the N/C ratio on cell cycle length, we found that the length of the S phase across the metasynchronous division rounds negatively correlated with cell volume (Fig. 4a,b). Therefore, we hypothesized that an AP–margin gradient of cell volumes in the cleavage-stage embryo might be responsible for unequally lengthening cell cycles from the AP to the margin. To test this hypothesis, we measured cell volumes by semiautomatically segmenting surface cells at the 128-cell stage (division round 8). Indeed, we found that, on average, cells closer to the AP were significantly larger than those away from it (Figs. 3a and 4g). To determine at what stage such a volume gradient first becomes apparent, we also measured N/C in embryos at the 8-cell stage (division round 4) and the 16-cell stage (division round 5)—the first stages in which cells can be classified as being 'central' or 'peripheral' based on their position. Interestingly, we observed that cells, but not nuclei, closer to the AP were consistently larger than the marginal cells, leading to central cells typically exhibiting a smaller N/C ratio than peripheral cells (Fig. 3b,c and Extended Data Fig. 5). Furthermore, the cell volume gradient not only persisted but was also further enhanced by subsequent cell divisions, as mother cells having unequal sizes themselves again divided asymmetrically to produce yet unequally sized daughters, thereby further diversifying cell volumes through cell lineage in addition to the already established position-driven cell volume diversity (Fig. 3d). For such unequal cell divisions to robustly give rise to a gradient in cell volumes along the AP–margin axis, upon division, the daughter cell closer to the AP must be, on average, larger than the daughter cell further from the AP. In line with this, we found that cell divisions in the early cleavage stages showed a tendency to produce larger daughter cells closer to AP, with the central daughter cell (closer to AP) being, on average, ~12.4% larger by volume than its peripheral sister cell (away from the AP) (Fig. 3e).

To determine what causes such patterned asymmetric cell divisions, we investigated how cell divisions are oriented and the cleavage plane positioned in the early embryo. Although several sophisticated models have been proposed to explain the orientation and positioning of the cleavage plane across systems, we started by first testing if following the simplest model, the ~140-year-old Hertwig's rule, can recapitulate the experimentally observed pattern of asymmetry[27,28]. More specifically, we assumed that the mitotic spindle in dividing blastomeres would orient along the longest cell axis, thereby dividing the cell along this axis. To test if such a geometry-driven mechanism would suffice to generate the observed pattern of asymmetric cell divisions and, therefore, the cell volume gradient, we predicted daughter cell volumes at the 16-cell stage by first identifying the longest axes of segmented cells at the 8-cell stage through principal component analysis and then bisecting them to obtain two daughter cells from each division[29] (Fig. 3e). Indeed, we found that with this approach, the predicted asymmetry in the daughter cell size closely matched the observed asymmetry for most cell divisions, such that the central daughter cells (closer to the AP) at the 16-cell stage were, on average, ~18.5% larger than their peripheral sister cells (further away from the AP) by volume (Fig. 3e). Importantly, this tendency of central daughter cells being bigger than peripheral ones is determined by the specific geometry of the first cell of the fertilized egg, the blastodisc, which is delineated not only by a plasma membrane at its outer side but also by the interface to the yolk granules on its inner side[11,30]. As the interface to the yolk granules is curved, the first two cell divisions will give rise to equally sized daughter cells that are more pointed and narrow at their peripheral ends. Dividing these cells again along their long axis will then, as a result, generate daughter cells in which the central cell is larger than the peripheral one. This suggests that a gradient of cell volumes along the AP–margin axis in the cleaving embryo can be explained by the specific geometry of the first cell in the fertilized egg, leading to unequal cell division along the AP–margin axis during subsequent division rounds.

Cell volume gradient causes patterned cell cycle lengthening along the AP–margin axis

Although the influence of cell volume on cell cycle length has been established in several systems, its role in zebrafish embryos remains unclear due to conflicting reports regarding the determinative effect of cell size in this context[14,16]. To unequivocally establish the contribution of cell volume—and, by extension, the N/C ratio—to the regulation of cell cycle length, we first increased the N/C ratio at the 1-cell stage by aspirating cytoplasm from the blastodisc (Fig. 4c). Consistent with the known role of elevated N/C ratios in prolonging cell cycles, we observed that, across different embryos, the S phase either lengthened prematurely or showed greater lengthening during division round 10, and the cell cycles desynchronized earlier than in control embryos (Fig. 4d). To test the converse, we decreased the N/C ratio by replicating a previous experiment[14], aspirating one nucleus from embryos at the 2-cell or 4-cell stage (Fig. 4e). In these embryos, only the control half—containing the nucleus—underwent initial cleavages, whereas no divisions occurred in the enucleated half (Fig. 4e and Supplementary Video 6). However, in a subset of embryos, nuclei from the control half eventually invaded the enucleated half around division round 4 or 5, prompting the onset of cleavages in that region (Fig. 4e and Supplementary Video 6). In particular, although all nuclei had undergone the same number of division cycles by this stage, those in the previously enucleated half now resided in a substantially larger cytoplasmic volume—comparable to the blastomere volume of cells three to four divisions earlier—and, therefore, had a lower N/C ratio. Consistent with earlier findings, these nuclei did not exhibit S-phase lengthening during division round 10—the point at which cell cycles typically begin to desynchronize in the control half, but instead continued to cycle metasynchronously. This, in line with previous observations of delayed and premature cell cycle lengthening in haploid and tetraploid embryos, respectively, supports the notion that a higher N/C ratio promotes S-phase lengthening and contributes to the onset of cell cycle desynchronization beyond division round 10 (ref. 14; Fig. 4f). However, it should be noted that although our analyses establish a deterministic role of N/C in S-phase length, they do not entirely exclude

https://doi.org/10.1038/s41567-025-03122-1

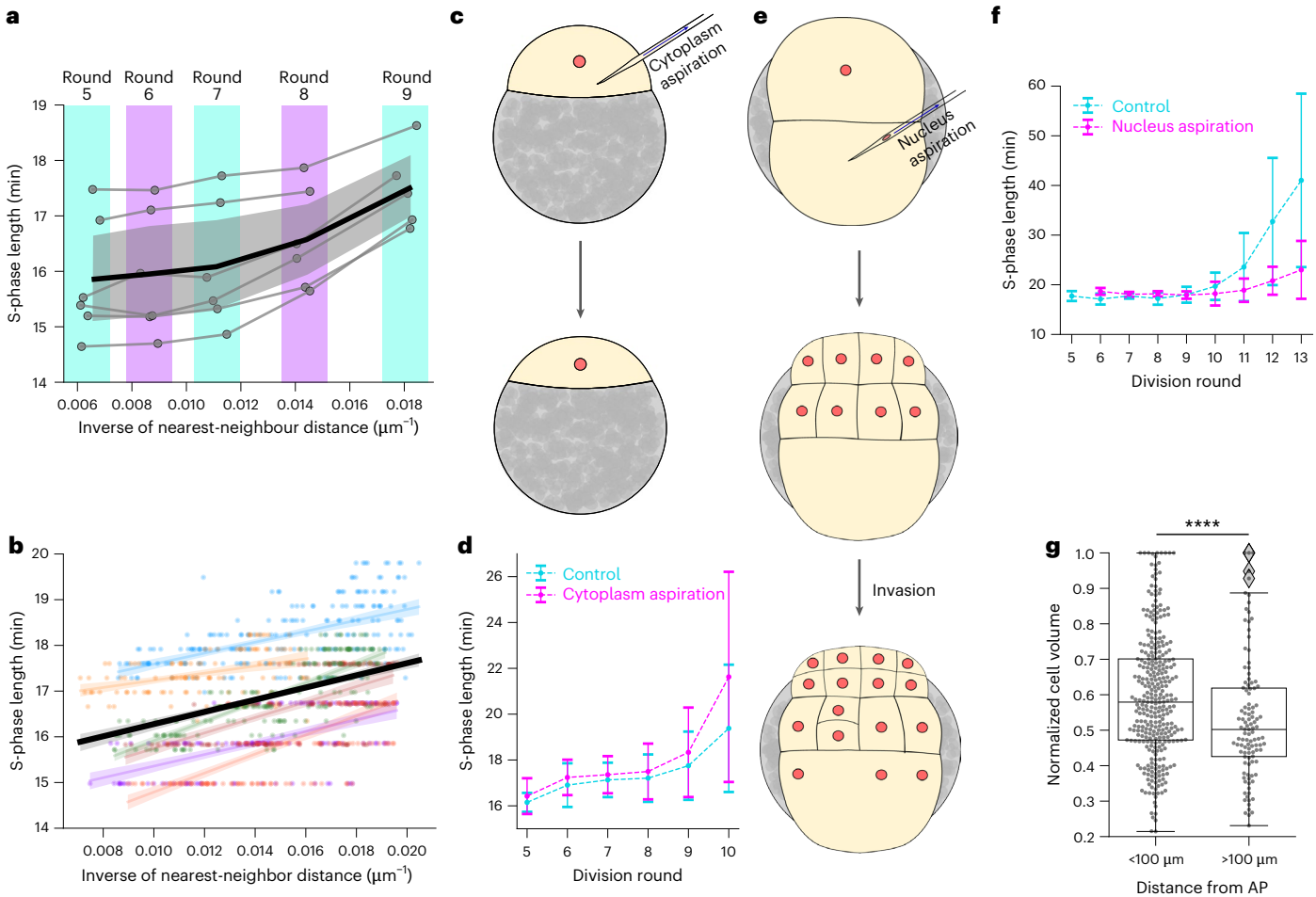

Fig. 4 | Cell volume regulates S-phase length. a, Line plots showing mean S-phase lengths in individual (thin, grey lines) and across (thick, black line, mean ± 95% confidence interval) embryos as a function of the inverse of the mean nearest-neighbour distance (mean of 3) in the metasynchronous cell cycle stages. Division rounds are indicated by the colour-bands overlaid on the dots ($n = 6$ embryos). **b**, Linear regression plots showing the relationship between the inverse of the nearest-neighbour distance (mean of 3) for each cell and the length of its S phase. Dots represent single cells, whereas the lines show the best-fit linear curve for the data. Each colour represents data for a unique embryo. The thick, black line shows a summary best fit for the data of all cells across all embryos. For each embryo, cells only within the 5th–95th percentile of their nearest-neighbour distances and S-phase length were considered for the analysis, which minimizes erroneous measurements at the extremes but also underestimates the relationship ($n = 6$ embryos, 964 cells). **c**, Schematic of the experiment in which a fraction of the cytoplasm was aspirated from the blastodisc within approximately 10 min before the first cell division to increase the N/C ratio. **d**, Representative line plot showing the S-phase length in each division round in control embryos and embryos from which the cytoplasm was aspirated (mean ± s.d., $n = 3$ embryos). **e**, Schematic of the experiment in which one of the nuclei at the 2-cell stage was aspirated to decrease the N/C ratio in the aspirated half of the embryo (top). Only the nucleated, control half initially develops (that is, shows mitotic cycles) (middle) until nuclei from this half invade the enucleated half (bottom), which then begins to develop with a smaller N/C ratio. **f**, Representative line plot showing S-phase length in each division round in the control and enucleated halves of the embryo depicted in **e** (mean ± s.d., $n = 3$ embryos). **g**, Box plot showing normalized cell volumes as a function of cell position with respect to the AP. Cell volumes were internally normalized by dividing each cell volume by the volume of the largest cell in the embryo. Each dot represents the data for an individual cell. Data are the same as in Fig. 3a, but the cells here have been classified into only two bins. The box in the box plot represents the middle 50% of the distribution, with the line representing the median and the whiskers indicating the minima and maxima. $n = 432$ cells, 11 embryos; two-tailed Student's t-test, $^{****}P = 0.001$.

the possibility that additional geometry- or N/C-independent mechanisms may also influence the S-phase length.

Having confirmed that the N/C ratio, in principle, can influence the S-phase length, we asked how perturbing the embryo-scale cell volume gradient within the cleaving embryo would affect the cell cycle (meta)synchrony and, consequently, the mitotic wave. To alter the cell volume gradient, we first generated bilobed embryos, displaying two ectopic (morphological) APs, by mounting 2-cell stage embryos in low-melting-point agarose (0.67% w/v in E3 buffer) when the first cytokinesis was in progress (Fig. 5a). We reasoned that spatially confining and, therefore, reshaping the embryo in this manner would produce larger cells away from the AP at the two ectopic APs. Interestingly, we found that not only the gradient of cell volumes was reshaped in the embryo but also that two mitotic waves emerged, one from each of the two ectopic APs, supporting the notion that the cell volume gradient is linked to the emergence of the mitotic wave (Fig. 5a,b and Supplementary Video 7).

Not only does cell size decrease along the AP–margin axis but also the proximity of cells to the yolk increases. This raises the possibility that yolk-derived factors, in addition to or alternatively to cell size, might influence the gradient in cell cycle length. However, direct cytoplasmic connectivity with the yolk is largely confined to the most marginal cells, making it unlikely to account for a cell cycle length gradient across the entire AP–margin axis[11]. To directly assess the effect of yolk proximity, we analysed correlations between division timing, cell size and yolk distance in bilobed embryos, where cell size

https://doi.org/10.1038/s41567-025-03122-1

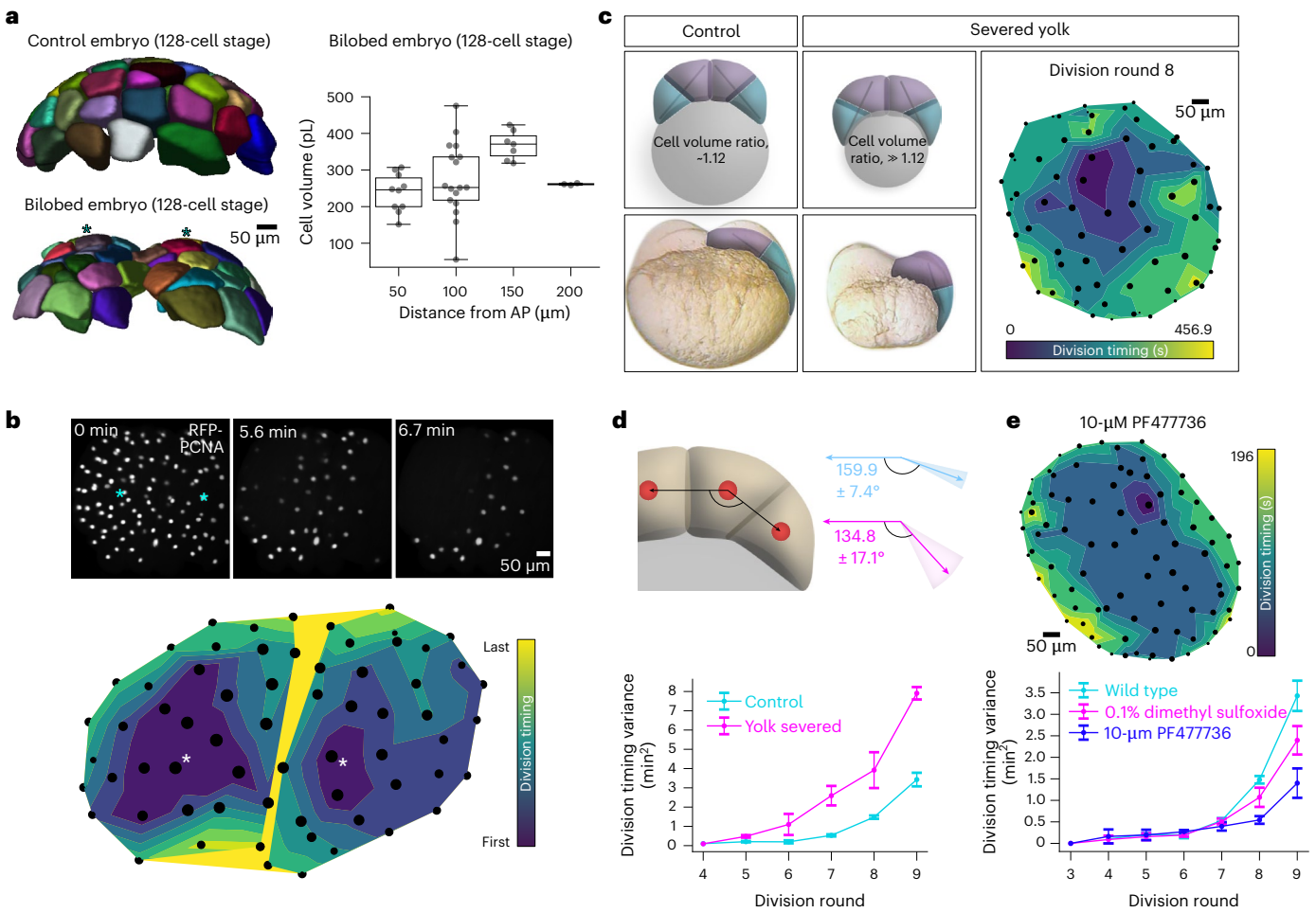

Fig. 5 | AP–margin cell volume gradient increases cell cycle metasynchrony in a Chek1-dependent manner. a, Representative images of 128-cell stage (division round 8) control and bilobed embryos with surface cells segmented (left) and box plot showing cell volumes as a function of the cell position with respect to the AP (right) for this bilobed embryo. Cyan asterisks mark the ectopic APs in the bilobed embryo. The box in the box plot represents the middle 50% of the distribution, with the line representing the median and the whiskers indicating the minima and maxima. $n = 37$ cells, representative of five embryos. **b**, Montage of images (top) and a contour plot (bottom) showing the propagation of mitotic waves in a representative bilobed Tg(*actb2:rfp-pcna*) embryo at division round 8. Asterisks mark the ectopic APs in the bilobed embryo ($n = 5$ embryos). **c**, Schematic (top-left) and representative (bottom-left) images of a control embryo and an embryo in which the yolk has been severed at the 2-cell stage to increase the curvature of the blastoderm-to-yolk cell interface. Lines inside the cells indicate the longest cell axis along which the divisions (division round 3) are expected to occur. Cells marked in magenta and cyan represent the resulting central and marginal daughter cells, respectively. The contour plot (right) shows mitotic wave propagation in division round 8 of a yolk-severed embryo (AP view). **d**, Schematic (top) of the decreased angle of cell divisions in division round 4 in yolk-severed embryos due to an increased curvature of the blastoderm-to-yolk cell interface compared with the corresponding control embryos. Angles are represented as mean ± s.d.; $n = 10$ and 14 cells for control and yolk-severed embryos, respectively). Line plot (bottom) showing the variance in cell division timings in control and yolk-severed embryos (mean ± s.e.m.; $n = 4$ embryos). **e**, Representative contour plot (top) showing mitotic wave propagation in a Chek1 inhibitor (PF477736)-treated embryo in division round 8 (AP view). Line plot (bottom) showing the variance in cell division timings in control and PF477736-treated embryos (mean ± s.e.m.; $n = 4$ embryos).

and position relative to the margin are changed. Consistent with our model, smaller cells divided later than larger cells regardless of their AP–margin position (Extended Data Fig. 6), arguing against a primary role for the yolk in regulating division timing.

To further challenge the role of embryo-wide cell size gradients in generating mitotic waves, we removed a part of the yolk on the vegetal side of the 2-cell stage embryo to increase the curvature of the blastodisc (the two blastomeres positioned on the yolk cell; Fig. 5c). On the basis of our analysis indicating that the cell volume gradient is a product of the curvature of the blastodisc–yolk interface, we reasoned that this increased curvature would reorient the longest axes of the two cells, such that they align more along the animal–vegetal axis, which would then amplify the volume asymmetry of cleavage divisions and, consequently, the phase difference between cell cycles (Fig. 5c). Strikingly, we found that in yolk-severed embryos, with cell divisions more aligned along the animal–vegetal axis, the mitotic wave indeed showed a greater cell division timing variance compared with the control embryos (Fig. 5c,d and Supplementary Video 8). Taken together, these observations strongly support the idea that a gradient of cell volume along the AP–margin axis, guided by embryo geometry, causes the generation of a gradient of S-phase lengths along the AP–margin axis of the blastoderm, thereby generating radial mitotic waves in the zebrafish embryo.

Among the major responders to a high N/C ratio is Chek1, which, when active, delays the S–M transition[7,25,31]. Although cell cycles have been shown to lengthen independently of Chek1 in *Xenopus* egg extracts, recent in vivo studies in *Drosophila* embryos have established it as a central factor that not only controls the mitotic wave speed but also regulates the desynchronization of cell cycles in embryos with heterogeneous N/C[7,26,31]. Therefore, we enquired whether Chek1 mediates the effect of cell volume on S-phase length. To that end, we inhibited Chek1 activity by treating embryos with 10 µM of PF477736,

https://doi.org/10.1038/s41567-025-03122-1

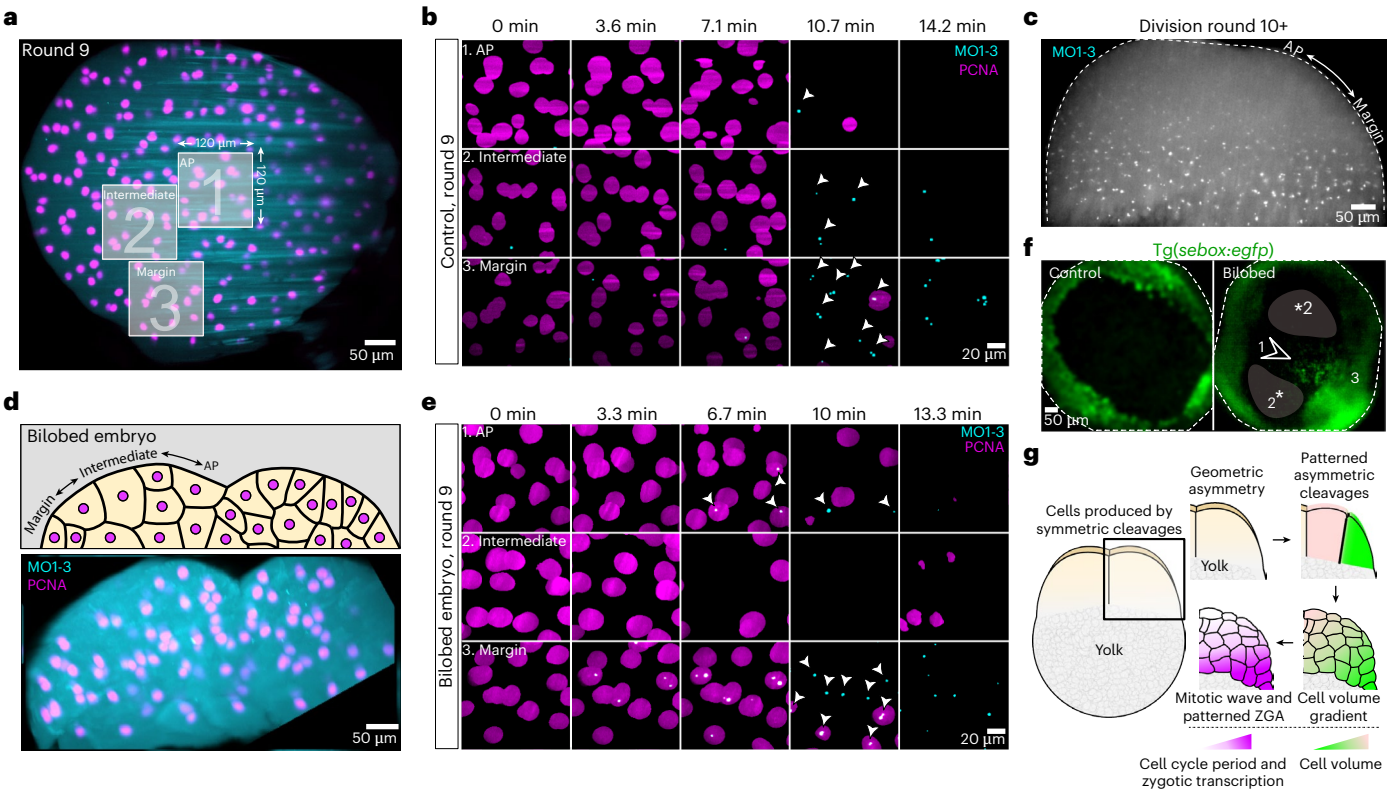

Fig. 6 | Zygotic transcription is initiated in a patterned manner along the AP–margin axis. a, Representative maximum intensity projection image showing the AP view of a control Tg(*actb2:rfp-pcna)* embryo injected with MO1-3-fluorescein in division round 9. Cyan, MO1-3-fluorescein; magenta, nuclei (PCNA). The three insets, each 120 µm × 120 µm in size, demarcate the regions (1, AP; 2, intermediate region; 3, margin) whose higher-magnification images are shown in **b** and **e**. **b**, Zoomed-in views of the insets shown in **a**. Cyan dots, marked with white arrowheads, represent nascent *mi430* transcripts detected by MO1-3-fluorescein. MO1-3 foci without an overlapping nuclear signal indicates that the cell is in mitosis ($n = 4$ embryos). **c**, Lateral view of a control embryo in division round 10 injected with MO1-3-fluorescein. **d**, Schematic (top) and a representative orthogonal maximum intensity projection image (bottom) of a bilobed Tg(*actb2:rfp-pcna)* embryo injected with the MO1-3-fluorescein embryo in division round 9. Cyan, MO1-3-fluorescein; magenta, nuclei (PCNA). **e**, Zoomed-in views of the equivalent regions (1, AP; 2, intermediate region; 3, margin) demarcated in **a** for a bilobed embryo in division round 9. Cyan dots represent nascent *mi430* transcripts. MO1-3 foci without an overlapping nuclear signal indicates that the cell is in mitosis ($n = 3$ embryos). **f**, AP view of control and bilobed Tg(*sebox:egfp*) embryos, with comparable regions from **a** indicated in the bilobed embryo. The arrowhead indicates the presence of ectopic *sebox:egfp* expression at the original AP, where a valley is formed between the two domes (ectopic APs) of the bilobed embryo. White asterisks indicate the positions of the ectopic APs. **g**, Schematic representing the geometry-driven asymmetric cell division patterning in the early embryo. Patterned asymmetric divisions generate a gradient of cell volume, producing mitotic phase waves and spatially patterning ZGA onset along the AP–margin axis.

a specific Chek1 activity inhibitor[32]. If Chek1 activity is required for the gradual metasynchronization of cell cycles through unequal S-phase lengthening, the cell cycle progression would be expected to show lesser variation in the treated embryos. Consistent with this, we found that, although Chek1-inhibited embryos produced mitotic waves like those in control embryos, they indeed exhibited a lower mitotic division timing variance (Fig. 5e and Supplementary Video 9). This suggests that Chek1 activity is critical for translating a cell volume gradient into a mitotic wave along the AP–margin axis of the blastoderm.

Cell volume and cell cycle period gradients pattern zygotic genome activation and germ layer specification along the AP–margin axis

Finally, we asked whether the geometry-derived cell volume gradient—and the resulting patterned mitotic metasynchrony—plays a developmental role that extends beyond the cleavage stages and impacts subsequent embryogenesis. In zebrafish embryos, mitotic metasynchrony diminishes in parallel with the onset of zygotic genome activation (ZGA), a pivotal process that lays the foundation for cell fate heterogeneity and is central to metazoan development[14]. Given previously reported roles of cell volume (N/C ratio promotes ZGA) and cell cycle length (shorter cell cycle prevents ZGA) in regulating ZGA, we investigated whether the observed gradient in cell volume and mitotic metasynchrony influences the onset of zygotic transcription[33–38]. To address this, we tracked the timing and spatial pattern of zygotic transcription initiation by imaging endogenous pri-*miR430* transcripts using the morpholino visualization of expression[39] (Fig. 6a). *miR430* genes are among the earliest and most abundantly transcribed genes during zebrafish ZGA, making them ideal markers for assessing transcriptional onset[40,41].

In most embryos, we observed the first signs of *miR430* transcription during division round 9. In particular, during rounds 9 and 10, transcription was initiated in a graded manner: *miR430* transcription foci first appeared—and/or persisted longer—in cells near the blastoderm margin. They then emerged in an intermediate zone between the margin and the AP, and finally in cells located at the AP (Fig. 6b,c, Extended Data Fig. 7 and Supplementary Videos 10 and 11). These findings suggest that zygotic transcription begins as a spatiotemporal gradient along the AP–margin axis, with marginal cells exhibiting higher transcriptional activity or competence than AP cells over the course of one to two division rounds. To determine whether this pattern of ZGA onset is driven by the underlying gradients in cell volume and/or cell cycle length, we examined bilobed embryos in which both of these gradients are perturbed (Figs. 5a,b and 6d). In contrast

to control embryos, cells at the AP in bilobed embryos are smaller and cycle more slowly than those in the intermediate zone (Fig. 5a,b). Remarkably, in these embryos, *miR430* transcription was initiated first at both the margin and the AP—where cells are the smallest—before appearing in the intermediate region (Fig. 6e and Supplementary Video 12). These results suggest that the gradient of cell volume and/or cell cycle length along the AP–margin axis influences the spatiotemporal onset of zygotic transcription. Thus, early embryo geometry can be linked directly to the initiation of zygotic gene expression, providing a mechanistic bridge between physical form and transcriptional timing in early development.

To determine whether the geometry-derived transcriptional gradient within the embryo plays a role in embryonic development, we asked whether altering the spatiotemporal pattern of ZGA onset in bilobed embryos would affect the specification of the first cell fates within the blastoderm. To investigate this, we used *Tg(sebox:egfp)* embryos to visualize the earliest mesendoderm progenitors, specified at the onset of gastrulation[42,43]. In control embryos, mesendoderm progenitors were exclusively specified at the blastoderm margin—the region in which ZGA is first initiated. By contrast, approximately 30% of bilobed embryos exhibited mesendoderm progenitors not only at the margin but also ectopically within the 'valley' between the two domes, reflecting the altered ZGA pattern in these embryos (Fig. 6f). These findings suggest that zygote geometry triggers a cascade of developmental events necessary for correct cell fate specification—an essential aspect of ensuring developmental robustness (Fig. 6g).

Discussion

Previous studies have shown that the shape of the zebrafish egg—particularly the blastodisc, the region from which all embryonic cells and tissues originate—is established by ooplasmic streaming, which segregates yolk granules from the cytoplasm within the fertilized egg[30,44]. Building on this, our findings suggest that the initial shape of the blastodisc drives asymmetric cell divisions during successive reductive cleavages by guiding mitotic spindle orientation, based on the simple premise that the spindle consistently aligns with the cell's longest axis, as described by Hertwig's rule[27,28,45]. These asymmetric divisions progressively generate a gradient of cell volumes along the AP–margin axis of the developing blastoderm, which, in turn, influences both cell cycle progression and ZGA along the same axis. Although we do not rule out the potential contribution of more complex mechanisms linking blastodisc shape to asymmetric cell divisions—such as differential interactions between spindle microtubules and yolk granules, the cell cortex or the plasma membrane—our results suggest that such factors are not required to explain the emergence of asymmetric divisions. Thus, the formation of a gradient in cell volume, as well as the consequent regulation of cell cycle dynamics and ZGA patterns, appears to be a direct outcome of the blastodisc's geometry.

Interestingly, our data connect the observed gradients in cell volume and/or cell cycle length to the onset of ZGA. This aligns with recent findings in *Xenopus* embryos, where ZGA is first initiated in the smaller cells at the AP[38]. Multiple molecular mechanisms have been proposed to explain the link between cell cycle length and the onset of ZGA, including the titration of cytoplasmic transcriptional repressors as the N/C ratio increases, and/or progressively lengthening cell cycles that permit sustained zygotic transcription. Our observation that smaller, slower-cycling cells at the margin are transcriptionally more active, initiating transcription first and retaining the transcription foci longer (Extended Data Fig. 7), suggests that both mechanisms may contribute to the regulation of zygotic gene activation.

We have previously shown that radially patterned cell behaviours and asymmetric tissue compaction along the AP–margin axis of the blastoderm emerge at the onset of gastrulation, providing essential conditions for proper morphogenetic movements during this stage of development[20,46]. It is plausible that these differences in tissue properties originate from distinct transcriptional profiles and cell fate specification, which are themselves driven by the differential patterns of ZGA, and ultimately embryo geometry, as described in this study.

The dependence of cell fate marker expression on early embryo geometry raises a central question: how do noisy gradients in cell size, cell cycle and transcriptional activity yield robust fate specification? Although individual fate markers may be regulated by distinct mechanisms, their spatial patterns probably emerge from the integration of cellular dynamics with physical constraints. For example, although Nodal signals, inducing mesendodermal cell fates within the blastoderm margin, originate in the yolk, proper Nodal reception in blastoderm cells requires zygotically expressed factors such as the co-receptor *oep*[47]. Margin cells, which undergo earlier ZGA, may, therefore, respond more strongly to Nodal due to an earlier and/or higher co-receptor expression, sharpening mesendodermal marker expression near the margin. In bilobed embryos, altered cell size, cell cycle and transcription patterns could shift this sensitivity—elevated transcription in the valley between the two lobes might allow cells to respond to lower Nodal levels and, consequently, adopt a mesendodermal cell fate. Thus, biochemical and molecular prepatterning, achieved by cellular properties such as cell cycle, size and transcriptional activity, may provide the foundation for robust cell fate specification.

Our findings, thus, establish a probable mechanistic link between two critical developmental milestones: the determination of blastodisc geometry immediately after fertilization and the onset of asymmetric tissue fluidization during gastrulation. This connection is further supported by our earlier observation that asymmetric tissue fluidization depends on proper mesendoderm specification[20,46], as well as by our current finding that embryos with perturbed geometry exhibit mesendodermal fate misspecification that parallels the altered pattern of ZGA onset. This suggests that inherent geometric asymmetries in blastodisc shape can have long-lasting developmental consequences, manifesting only later as their effects accumulate during the early proliferative phase of embryogenesis.

Consistent with this notion, several other organisms—including *Caenorhabditis elegans*, sea urchins and *Xenopus*—exhibit alignment between axes of cell cycle length and/or cell volume and the axes along which germ layer fates diverge, underscoring the developmental significance of geometry-derived patterns as robust and reproducible determinants of embryonic organization. Nonetheless, the specific outcomes of this fundamental relationship are likely to vary across species and must be examined within the unique developmental context of each organism.

Online content

Any methods, additional references, Nature Portfolio reporting summaries, source data, extended data, supplementary information, acknowledgements, peer review information; details of author contributions and competing interests; and statements of data and code availability are available at https://doi.org/10.1038/s41567-025-03122-1.

References

1. Luciano, M. et al. Cell monolayers sense curvature by exploiting active mechanics and nuclear mechanoadaptation. *Nat. Phys.* **17**, 1382–1390 (2021).
2. Cheikh, M. I. et al. A comprehensive model of *Drosophila* epithelium reveals the role of embryo geometry and cell topology in mechanical responses. *eLife* **12**, e85569 (2023).
3. Lou, Y., Rupprecht, J.-F., Theis, S., Hiraiwa, T. & Saunders, T. E. Curvature-induced cell rearrangements in biological tissues. *Phys. Rev. Lett.* **130**, 108401 (2023).
4. Luciano, M., Tomba, C., Roux, A. & Gabriele, S. How multiscale curvature couples forces to cellular functions. *Nat. Rev. Phys.* **6**, 246–268 (2024).

5. Gehrels, E. W., Chakrabortty, B., Perrin, M.-E., Merkel, M. & Lecuit, T. Curvature gradient drives polarized tissue flow in the *Drosophila* embryo. *Proc. Natl Acad. Sci. USA* **120**, e2214205120 (2023).
6. Lefebvre, M. F., Claussen, N. H., Mitchell, N. P., Gustafson, H. J. & Streichan, S. J. Geometric control of myosin II orientation during axis elongation. *eLife* **12**, e78787 (2023).
7. Deneke, V. E., Melbinger, A., Vergassola, M. & Di Talia, S. Waves of Cdk1 activity in S phase synchronize the cell cycle in *Drosophila* embryos. *Dev. Cell* **38**, 399–412 (2016).
8. Vergassola, M., Deneke, V. E. & Di Talia, S. Mitotic waves in the early embryogenesis of *Drosophila*: bistability traded for speed. *Proc. Natl Acad. Sci. USA* **115**, E2165–E2174 (2018).
9. Chang, J. B. & Ferrell, J. E. Mitotic trigger waves and the spatial coordination of the *Xenopus* cell cycle. *Nature* **500**, 603–607 (2013).
10. Anderson, G. A., Gelens, L., Baker, J. C. & Ferrell, J. E. Desynchronizing embryonic cell division waves reveals the robustness of *Xenopus laevis* development. *Cell Rep.* **21**, 37–46 (2017).
11. Kimmel, C. B., Ballard, W. W., Kimmel, S. R., Ullmann, B. & Schilling, T. F. Stages of embryonic development of the zebrafish. *Dev. Dyn.* **203**, 253–310 (1995).
12. Zamir, E., Kam, Z. & Yarden, A. Transcription-dependent induction of G1 phase during the zebra fish midblastula transition. *Mol. Cell. Biol.* **17**, 529–536 (1997).
13. Boothe, T. et al. A tunable refractive index matching medium for live imaging cells, tissues and model organisms. *eLife* **6**, e27240 (2017).
14. Kane, D. A. & Kimmel, C. B. The zebrafish midblastula transition. *Dev. Camb. Engl.* **119**, 447–456 (1993).
15. Keller, P. J., Schmidt, A. D., Wittbrodt, J. & Stelzer, E. H. K. Reconstruction of zebrafish early embryonic development by scanned light sheet microscopy. *Science* **322**, 1065–1069 (2008).
16. Olivier, N. et al. Cell lineage reconstruction of early zebrafish embryos using label-free nonlinear microscopy. *Science* **329**, 967–971 (2010).
17. Berloco, M., Fanti, L., Breiling, A., Orlando, V. & Pimpinelli, S. The maternal effect gene, abnormal oocyte (abo), of *Drosophila melanogaster* encodes a specific negative regulator of histones. *Proc. Natl Acad. Sci. USA* **98**, 12126–12131 (2001).
18. Gunjan, A. & Verreault, A. A Rad53 kinase-dependent surveillance mechanism that regulates histone protein levels in *S. cerevisiae*. *Cell* **115**, 537–549 (2003).
19. Brown, D. T., Alexander, B. T. & Sittman, D. B. Differential effect of H1 variant overexpression on cell cycle progression and gene expression. *Nucleic Acids Res.* **24**, 486–493 (1996).
20. Petridou, N. I., Corominas-Murtra, B., Heisenberg, C.-P. & Hannezo, E. Rigidity percolation uncovers a structural basis for embryonic tissue phase transitions. *Cell* **184**, 1914–1928.e19 (2021).
21. Kuramoto, Y. *Chemical Oscillations, Waves, and Turbulence* Vol. 19 (Springer, 1984).
22. Kimmel, C. B. & Law, R. D. Cell lineage of zebrafish blastomeres: I. Cleavage pattern and cytoplasmic bridges between cells. *Dev. Biol.* **108**, 78–85 (1985).
23. Nolet, F. E. et al. Nuclei determine the spatial origin of mitotic waves. *eLife* **9**, e52868 (2020).
24. Murata-Hori, M., Tatsuka, M. & Wang, Y.-L. Probing the dynamics and functions of aurora B kinase in living cells during mitosis and cytokinesis. *Mol. Biol. Cell* **13**, 1099–1108 (2002).
25. Conn, C. W., Lewellyn, A. L. & Maller, J. L. The DNA damage checkpoint in embryonic cell cycles is dependent on the DNA-to-cytoplasmic ratio. *Dev. Cell* **7**, 275–281 (2004).
26. Piñeros, L. et al. The nuclear-cytoplasmic ratio controls the cell-cycle period in compartmentalized frog egg extract. *Curr. Biol.* **35**, 4426–4441.e6 (2025).
27. Minc, N., Burgess, D. & Chang, F. Influence of cell geometry on division-plane positioning. *Cell* **144**, 414–426 (2011).
28. Hertwig, O. *Das Problem der Befruchtung und der Isotropie des Eies: eine Theorie der Vererbung* (Verlag von Gustav Fischer, 1884).
29. Wold, S., Esbensen, K. & Geladi, P. Principal component analysis. *Chemom. Intell. Lab. Syst.* **2**, 37–52 (1987).
30. Shamipour, S. et al. Bulk actin dynamics drive phase segregation in zebrafish oocytes. *Cell* **177**, 1463–1479.e18 (2019).
31. Deneke, V. E. et al. Self-organized nuclear positioning synchronizes the cell cycle in *Drosophila* embryos. *Cell* **177**, 925–941.e17 (2019).
32. Danilova, N. et al. The role of the DNA damage response in zebrafish and cellular models of Diamond Blackfan anemia. *Dis. Model. Mech.* **7**, 895–905 (2014).
33. Newport, J. & Kirschner, M. A major developmental transition in early *Xenopus* embryos: I. Characterization and timing of cellular changes at the midblastula stage. *Cell* **30**, 675–686 (1982).
34. Newport, J. & Kirschner, M. A major developmental transition in early *Xenopus* embryos: II. Control of the onset of transcription. *Cell* **30**, 687–696 (1982).
35. Langley, A. R., Smith, J. C., Stemple, D. L. & Harvey, S. A. New insights into the maternal to zygotic transition. *Development* **141**, 3834–3841 (2014).
36. Edgar, B. A. & Schubiger, G. Parameters controlling transcriptional activation during early *Drosophila* development. *Cell* **44**, 871–877 (1986).
37. Kimelman, D., Kirschner, M. & Scherson, T. The events of the midblastula transition in *Xenopus* are regulated by changes in the cell cycle. *Cell* **48**, 399–407 (1987).
38. Chen, H., Einstein, L. C., Little, S. C. & Good, M. C. Spatiotemporal patterning of zygotic genome activation in a model vertebrate embryo. *Dev. Cell* **49**, 852–866.e7 (2019).
39. Hadzhiev, Y. et al. A cell cycle-coordinated polymerase II transcription compartment encompasses gene expression before global genome activation. *Nat. Commun.* **10**, 691 (2019).
40. Giraldez, A. J. et al. Zebrafish MiR-430 promotes deadenylation and clearance of maternal mRNAs. *Science* **312**, 75–79 (2006).
41. Heyn, P. et al. The earliest transcribed zygotic genes are short, newly evolved, and different across species. *Cell Rep.* **6**, 285–292 (2014).
42. Poulain, M. & Lepage, T. Mezzo, a paired-like homeobox protein is an immediate target of nodal signalling and regulates endoderm specification in zebrafish. *Development* **129**, 4901–4914 (2002).
43. Ruprecht, V. et al. Cortical contractility triggers a stochastic switch to fast amoeboid cell motility. *Cell* **1**, 673–685 (2015).
44. Roosen-Runge, E. C. On the early development—bipolar differentiation and cleavage—of the zebra fish, *Brachydanio rerio*. *Biol. Bull.* **75**, 119–133 (1938).
45. Middelkoop, T. C. et al. A cytokinetic ring-driven cell rotation achieves Hertwig's rule in early development. *Proc. Natl Acad. Sci. USA* **121**, e2318838121 (2024).
46. Petridou, N. I., Grigolon, S., Salbreux, G., Hannezo, E. & Heisenberg, C.-P. Fluidization-mediated tissue spreading by mitotic cell rounding and non-canonical Wnt signalling. *Nat. Cell Biol.* **21**, 169–178 (2019).
47. Gritsman, K. et al. The EGF-CFC protein one-eyed pinhead is essential for nodal signaling. *Cell* **97**, 121–132 (1999).

Publisher's note Springer Nature remains neutral with regard to jurisdictional claims in published maps and institutional affiliations.

Open Access This article is licensed under a Creative Commons Attribution 4.0 International License, which permits use, sharing, adaptation, distribution and reproduction in any medium or format,

as long as you give appropriate credit to the original author(s) and the source, provide a link to the Creative Commons licence, and indicate if changes were made. The images or other third party material in this article are included in the article's Creative Commons licence, unless indicated otherwise in a credit line to the material. If material is not included in the article's Creative Commons licence and your intended use is not permitted by statutory regulation or exceeds the permitted use, you will need to obtain permission directly from the copyright holder. To view a copy of this licence, visit http://creativecommons.org/licenses/by/4.0/.

© The Author(s) 2026

Methods

Cell cycle analysis

Tg(*actb2:rfp-pcna*) embryos were dechorionated and, at the desired stage, mounted in 0.5% agarose gels prepared in E3 buffer with the AP facing upwards in casts made with 2% agarose solution in E3 buffer[13]. RFP fluorescence was imaged at 23.5 °C using a 20× water-dipping objective on ZEISS LSM800 (numerical aperture of 0.8), LSM880 (numerical aperture of 1.0) or LSM900 (numerical aperture of 1.0) upright confocal microscopes. Then, 200–350-µm-thick *Z* stacks were acquired for different experiments with temporal resolutions ranging between 17 and 65 s per *Z* stack. The presence or absence of nuclear RFP-PCNA fluorescence was used to determine if a cell was in the S or M phase of the cell cycle, respectively[48–50]. The nuclear signal was segmented in Fiji (v. 2.16.0/1.54p; Java 1.8.0_172) using the Labkit plug-in (v. 0.4.0)[51,52]. The segmented objects were imported into Bitplane Imaris (v. 9.9) (https://imaris.oxinst.com/) to generate tracks and obtain tracking-related data, including track start time (S-phase entry), track end time (M-phase entry), track duration (S-phase length) and the nuclear coordinates at the last S-phase time point (position). These data were then analysed using the Pandas package (v. 1.5.3) in Python (v. 3.12.9) to calculate, for instance, the division timing variance in a given division round, followed by plotting using mainly the Matplotlib (v. 3.8.2) and seaborn (v. 0.12.2) packages[53–55].

Mitotic wave speed

The mitotic wave speed for a given division round was determined by first identifying the position of the wave origin and the timing of the wave origination, measuring all other nuclear distances and mitotic entry timings relative to this position and time, and then generating the best-fitting distance–time linear curve. In the cases where more than one nucleus could be considered the origin of the mitotic wave due to a simultaneous entry into mitosis, the mean of the 3D coordinates of such nuclei was considered as the position of wave origin. Furthermore, it should be noted that, especially during division rounds 2 and 3, the wave traverses the embryo nearly instantaneously, and in most of our experiments, we could not temporally resolve these early cell divisions, giving us infinite mitotic wave speeds. However, for analytical reasons, we only considered those embryos in which the divisions could be resolved, disregarding embryos exhibiting infinite speeds, which would provide an underestimate of the mitotic wave speed.

Microinjections

To visualize cell cycle progression using Histone 1 as the marker, 0.5 ng of Histone 1-Alexa Fluor 488 (catalogue number H13188, Invitrogen) was injected at the 1-cell stage into wild-type AB or Tg(*actb2:lyn-tdTomato*) embryos[56]. Mosaic perturbation of the cycling period of a subset of the cells was carried out by mounting 32/64-cell stage embryos in 2% agarose solution in E3 buffer and injecting 0.2–0.3 ng of Histone 1-Alexa Fluor 488 into such cells. *chek1* overexpression was achieved by injecting 12 pg *chek1* mRNA into the one-cell embryo[20,46]. mRNA was prepared as described previously[21]. To test the cellular connectivity at the 16- and 64-cell stages, 0.0625 ng of fluorescein isothiocyanate–carboxymethyl–dextran (40 kDa) was injected into a single cell at the desired stage, and the embryos were mounted and imaged as described above.

Drug treatments

Aurkb function was inhibited by transiently incubating dechorionated <5 min post-fertilization (mpf) embryos in 50 µM of AZD1152 (catalogue number SML0268, Sigma-Aldrich) solution for 15 min, after which they were returned to the E3 buffer. Embryos showing successful nuclear cycling despite a failure of cytokinesis were then imaged as described above. Inhibition of the Aurkb function concomitantly with the *chek1* overexpression or Histone 1-Alexa Fluor 488 visualization was performed by injecting 12 pg of *chek1* mRNA or 0.5 ng of Histone 1-Alexa Fluor 488, respectively, at the 1-cell stage, as described above, followed by incubation in the Aurkb inhibitor. Chek1 activity inhibition was performed by dechorionating <10-mpf embryos and incubating them in 10 µM of PF477736 (catalogue number HY-10032, MedChem Express) solution in E3 buffer throughout the duration of the analysis.

Nuclear volume measurement

Nuclear RFP-PCNA fluorescence was segmented from *Z* stacks by thresholding using Fiji (v. 2.16.0/1.54p; Java 1.8.0_172), and their volumes were measured using the 3D Objects Counter plug-in (v. 2.0.1)[57].

Cell volume and N/C measurements

Cell volumes at the 8- and 16-cell stages were measured by semiautomatically generating cell segmentation using the 'Contour' function for surface creation in Bitplane Imaris (v. 9.9) from *Z* stacks of Tg(*actb2:mCherry-CAAX*) embryos[58]. Once segmented, the physical attributes of individual cells, such as volume and position, were exported from Bitplane Imaris (v. 9.9) as CSV files. The last time point before the onset of the fourth or fifth mitotic round was used to measure the cell volume for the 8- or the 16-cell stage, respectively. Cell volumes at the 128-cell stage were measured by generating cell segmentations using the LimeSeg plug-in (v. 0.4.2) in Fiji (v. 2.16.0/1.54p; Java 1.8.0_172) and exporting the cell volume data for individual segmented objects[59]. All downstream data analysis was performed in Python (v. 3.12.9), mainly using the Pandas package (v. 1.5.3), and the plots were produced using the Matplotlib (v. 3.8.2) and seaborn (v. 0.12.2) packages. To directly measure the N/C for cells at the 8- and the 16-cell stages, *Tg(actb2:mCherry-CAAX)* embryos injected with 0.5 ng of Histone 1-Alexa Fluor 488 at the 1-cell stage were imaged as described above. Cell volumes were estimated by semiautomatically creating cell and nuclear surfaces in Imaris (v. 9.9), whose volumes were then used to determine the N/C ratio for each cell.

Daughter cell volume prediction

Cell surfaces generated in Bitplane Imaris (v. 9.9) at the 8-cell stage were exported as WRL files, imported into MeshLab (https://www.meshlab.net/), from where individual cell surfaces were exported as PLY files. These files were subsequently processed in Python (v. 3.12.9) to identify the longest cell axis by performing principal component analysis, along which the cell was bisected into two daughter cells representing cells at the 16-cell stage[29].

Nearest-neighbour distance calculation

Nuclei positions were obtained from Bitplane Imaris (v. 9.9), as detailed above. For each nucleus, the three nearest neighbours were identified, and their mean distance from the reference nucleus was calculated using the Pandas package (v. 1.5.3) in Python (v. 3.12.9).

Cytoplasm aspiration

At approximately 30 mpf, Tg(*actb2:rfp-pcna*) embryos were mounted in E3 buffer on a substrate prepared with 2% agarose solution in E3 buffer. A 20-µm blunt-end needle attached to a 10-µl Hamilton syringe was inserted through the yolk into the blastodisc, and the cytoplasm was carefully aspirated. The nuclear RFP-PCNA signal was constantly observed using a Leica stereofluorescence microscope to ensure the nucleus was not extracted together with the cytoplasm.

Nucleus aspiration

The setup and mounting procedure for nucleus aspiration were the same as for cytoplasm aspiration described above, except that, in this case, the nucleus was aspirated rather than the cytoplasm and from embryos at the 2-cell stage rather than the 1-cell stage. Care was exercised to ensure that the nucleus was extracted with a negligible volume of the cytoplasm being aspirated in the process.

Generation of bilobed embryos
Bilobed embryos were created by spatially confining dechorionated embryos at the 2-cell stage, still undergoing cytokinesis from division round 1, in 0.5%–0.6% agarose in E3 buffer. Microscopy was performed as described above.

Yolk severing
To sever the yolk, dechorionated embryos at the 2-cell stage were placed on a substrate of 3% methylcellulose in E3 buffer in a glass dish. Using an eyelash attached to the end of a Pasteur pipette, the vegetal half of the yolk was first punctured to prevent the embryo from exploding due to a build-up of internal pressure during the severing procedure, and then carefully sliced. The embryo was allowed to recover for at least 15 min after the procedure, followed by mounting and microscopy, as detailed above.

Cell division angle measurement
Four orthogonal sections, each showing four nuclei along the plane of division round 4 at the 16-cell stage, were generated using the reslice function in Fiji from *Z* stacks of individual Tg(*actb2:rfp-pcna*) embryos. The angles between the nuclei were then measured using Fiji (v. 2.16.0/1.54p; Java 1.8.0_172), as represented in Fig. 5d, to obtain the angle of cell divisions in division round 4.

miR430 transcription analysis
pri-*miR430* transcripts were labelled as described previously[39]. Tg(*actb2:rfp-pcna*) embryos injected with MO1-3-fluorescein (Gene Tools) at the 1-cell stage were mounted in 0.5% agarose solution in E3 buffer in #3 fluorinated ethylene propylene tubes, and the *Z* stacks were generated with a temporal resolution of approximately 1 min per *Z* stack using a 20×/1.33-numerical-aperture objective on a ZEISS Lightsheet 7 microscope. Maximum intensity projections of these time-lapse recordings were then used to assess the transcription status of the individual nuclei.

Ethics statement
All animal breeding and procedures were performed in accordance with the European Union animal welfare guidelines and involve only low-severity lines, in accordance with the authorized animal breeding licences (66018/8-II/3b/2013 and 2023-0.288.351) in the Institute of Science and Technology Austria Aquatics Facility (approval number 024-0.730.856). All experiments were performed before 5 days post-fertilization, a period during which zebrafish do not feed independently and in line with the principle of 3Rs.

Reporting summary
Further information on research design is available in the Nature Portfolio Reporting Summary linked to this article.

Data availability
Source data are provided with this paper. All other data that are necessary to interpret, verify and extend the research within this article are available from the corresponding author upon reasonable request.

Code availability
The code relevant to this article is available via GitHub at https://github.com/Irene-Li/MitoticWaves.

References

48. Budke, H. et al. Assessment of cell proliferation in paraffin sections of normal bone marrow by the monoclonal antibodies Ki-67 and PCNA. *Mod. Pathol.* **7**, 860–866 (1994).
49. Kelman, Z. PCNA: structure, functions and interactions. *Oncogene* **14**, 629–640 (1997).
50. Leung, A. Y. et al. Proliferating cell nuclear antigen (PCNA) as a proliferative marker during embryonic and adult zebrafish hematopoiesis. *Histochem. Cell Biol.* **124**, 105–111 (2005).
51. Schindelin, J. et al. Fiji: an open-source platform for biological-image analysis. *Nat. Methods* **9**, 676–682 (2012).
52. Arzt, M. et al. LABKIT: labeling and segmentation toolkit for big image data. *Front. Comput. Sci.* **4**, 777728 (2022).
53. McKinney, W. Data structures for statistical computing in Python. In *Proc. 9th Python in Science Conference* 56–61 (SciPy, 2010).
54. Hunter, J. D. Matplotlib: a 2D graphics environment. *Comput. Sci. Eng* **9**, 90–95 (2007).
55. Waskom, M. L. seaborn: statistical data visualization. *J. Open Source Softw.* **6**, 3021 (2021).
56. Stegmaier, J. et al. Real-time three-dimensional cell segmentation in large-scale microscopy data of developing embryos. *Dev. Cell* **36**, 225–240 (2016).
57. Bolte, S. & Cordelières, F. P. A guided tour into subcellular colocalization analysis in light microscopy. *J. Microsc.* **224**, 213–232 (2006).
58. Tavano, S. et al. BMP-dependent patterning of ectoderm tissue material properties modulates lateral mesendoderm cell migration during early zebrafish gastrulation. *Cell Rep.* **44**, 115387 (2025).
59. Machado, S., Mercier, V. & Chiaruttini, N. LimeSeg: a coarse-grained lipid membrane simulation for 3D image segmentation. *BMC Bioinform.* **20**, 2 (2019).

Acknowledgements
We thank N. Petridou (EMBL) for sharing results before publication. N.M. was supported by funding from the European Union's Horizon 2020 programme under the Marie Skłodowska-Curie COFUND Actions ISTplus grant agreement number 754411. Y.I.L. acknowledges funding from the European Union's Horizon 2020 research and innovation programme under the Marie Skłodowska-Curie grant agreement number 101034413. The research was supported by funding to C.-P.H. from the NOMIS Foundation, Project ID 1.844. We would like to thank past and present members of the Heisenberg and Hannezo groups for discussions, particularly S. Shamipour, V. Doddihal, M. Jovic, N. Hino, F. N. Arslan, R. Kobylinska and C. Camelo for feedback on the draft manuscript. This research was supported by the Scientific Service Units (SSU) of Institute of Science and Technology Austria through resources provided by the Aquatics Facility, Imaging & Optics Facility (IOF), Scientific Computing (SciComp) facility and Lab Support Facility (LSF).

Author contributions
N.M. and C.-P.H. conceptualized the study. All authors contributed to the design of the experiments. N.M. (experiments) and Y.I.L. (theory) acquired and analysed the data. N.M. and C.-P.H. prepared the paper with input and feedback from all authors.

Funding
Open access funding provided by Institute of Science and Technology (IST Austria).

Competing interests
The authors declare no competing interests.

Additional information
Extended data is available for this paper at https://doi.org/10.1038/s41567-025-03122-1.

Supplementary information The online version contains supplementary material available at https://doi.org/10.1038/s41567-025-03122-1.

Correspondence and requests for materials should be addressed to Carl-Philipp Heisenberg.

Peer review information *Nature Physics* thanks Stefano Di Talia and Nicolas Minc for their contribution to the peer review of this work.

Reprints and permissions information is available at www.nature.com/reprints.

https://doi.org/10.1038/s41567-025-03122-1

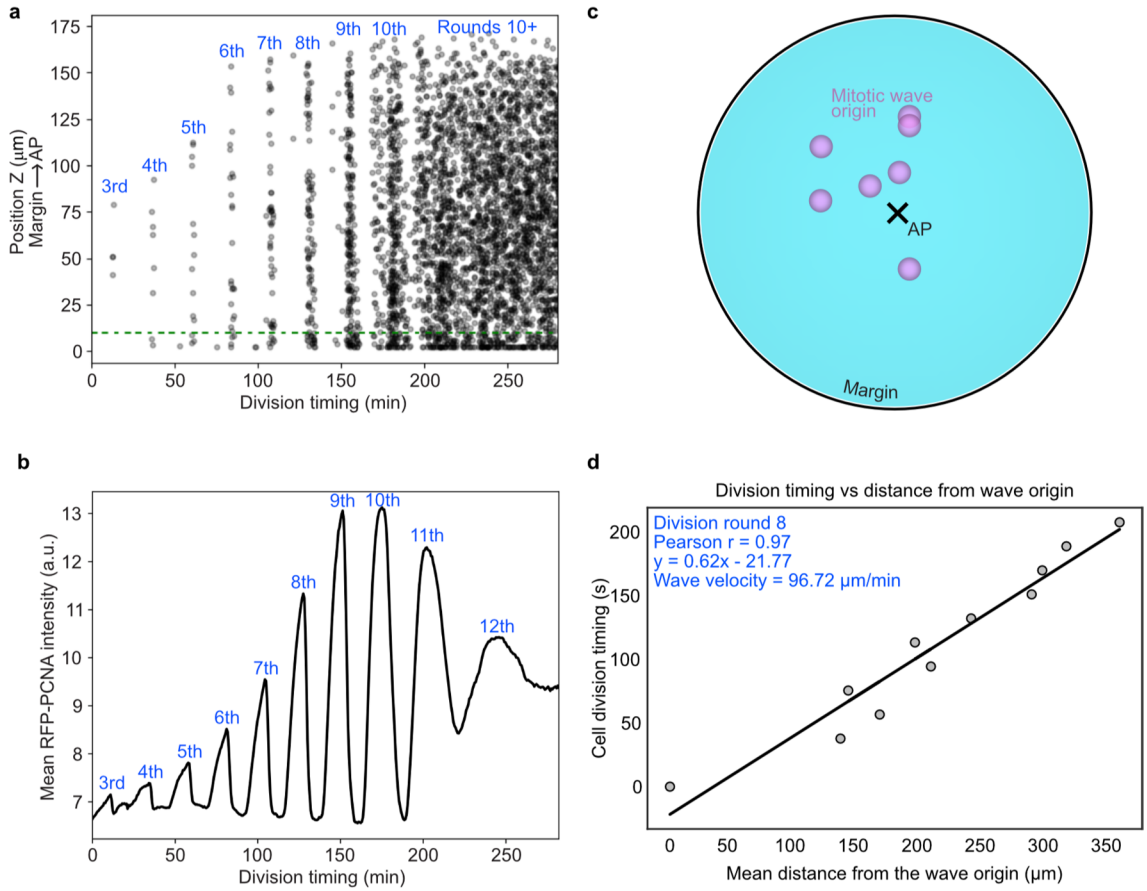

Extended Data Fig. 1 | Cells cycle periodically, and their division timings correlate linearly with their distance from the wave origin. (**a**) Scatter plot of division timing for individual cells starting at cleavage division round 3 (x-axis) relative to their position along the animal-margin axis (y-axis) for one representative wild-type embryo. The green dotted line outlines cells located at a distance of <10 µm from the bottom of the image stack that could not be reliably tracked. (**b**) Mean RFP-PCNA intensity, as a marker for mitosis onset, as a function of time. Mean PCNA intensity increases during the S-phase, peaks just before the S-M transition, and declines in the M-phase. Thus, a narrow peak indicates greater synchrony and vice versa. (**c**) Representative scheme showing the position of the mitotic wave origin in division round 8 (n = 7 embryos). (**d**) Representative plot of cleavage division timing as a function of cell distance from the mitotic wave origin in cleavage division round 8 from a wild-type embryo. Cells undergoing the S-M transition were binned together.

https://doi.org/10.1038/s41567-025-03122-1

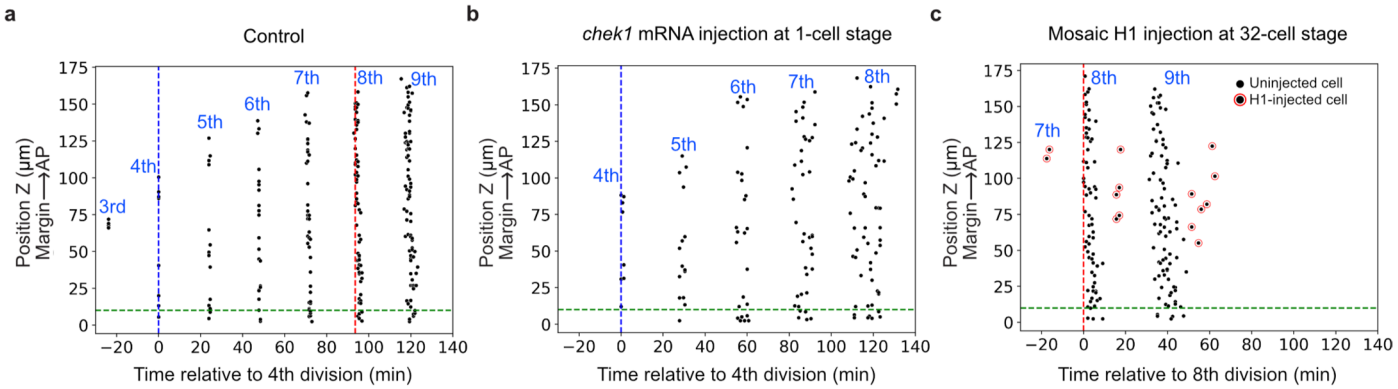

Extended Data Fig. 2 | Desynchronized cell cycles do not resynchronize during cleavages. Representative scatter plots of the division timing for individual surface cells relative to their position along the animal-margin axis in control embryos (**a**), and embryos injected with either 12 pg *chek1* mRNA at the 1-cell stage (**b**) or 0.3 ng Histone1 protein at the 32-cell stage (**c**). Blue and red dotted lines demarcate the onset of the 4th and 8th cleavage divisions, respectively. Green dotted line outlines cells located at a distance of <10 µm from the bottom of the image stack that could not be reliably tracked.

https://doi.org/10.1038/s41567-025-03122-1

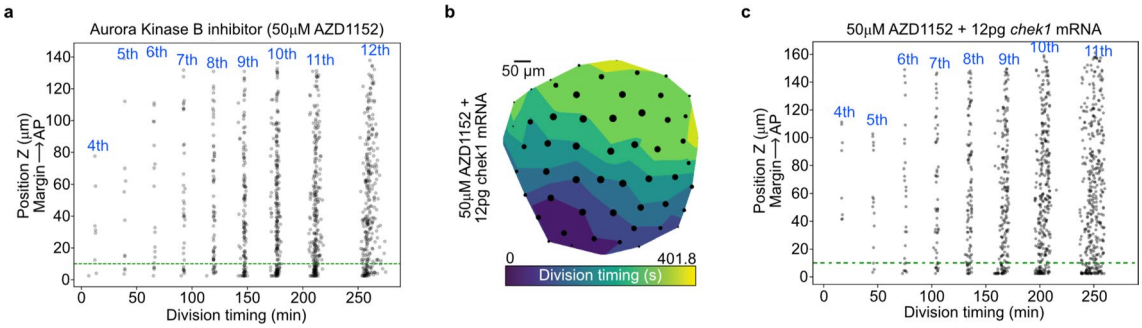

Extended Data Fig. 3 | Mitotic wave originates at the margin and persists after division round 10 in syncytial embryos. (**a**) Representative scatter plot of the division timings for individual cells relative to their position along the animal-margin axis in a syncytial Tg(*actb2:rfp-pcna*) embryo (n = 7 embryos). (**b**) Contour plot of the mitotic wave across all surface cells at the 8th round of cleavage division round in syncytialized Tg(*actb2:rfp-pcna*) embryos injected with 12 pg *chek1* mRNA at the one-cell stage, and (**c**) a scatter plot of division timings relative to position along the AP-margin axis for a representative syncytial embryo injected with 12 pg *chek1* mRNA. n = 4 embryos.

https://doi.org/10.1038/s41567-025-03122-1

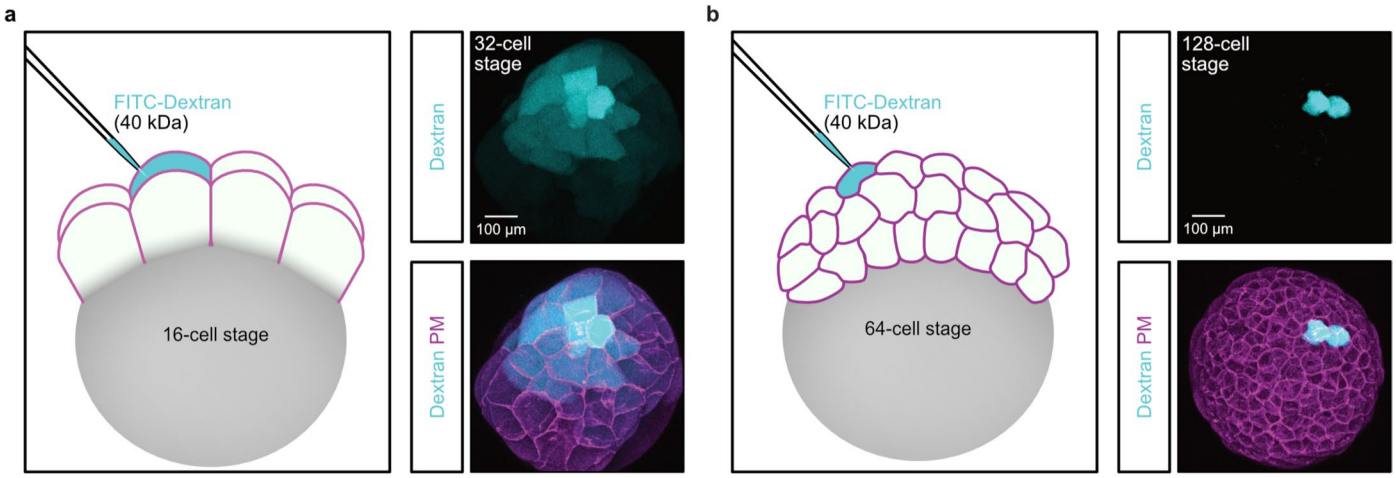

Extended Data Fig. 4 | Cellular connectivity decreases as the cleavage stages progress. A schematic each for single-cell injections of 40 kDa FITC-CM-Dextran at the 16- (**a**) and the 64-cell stage (**b**) in Tg(*actb2:mCherry-CAAX*) embryos and representative images one division round later (n = 3 and 6 embryos, respectively).

https://doi.org/10.1038/s41567-025-03122-1

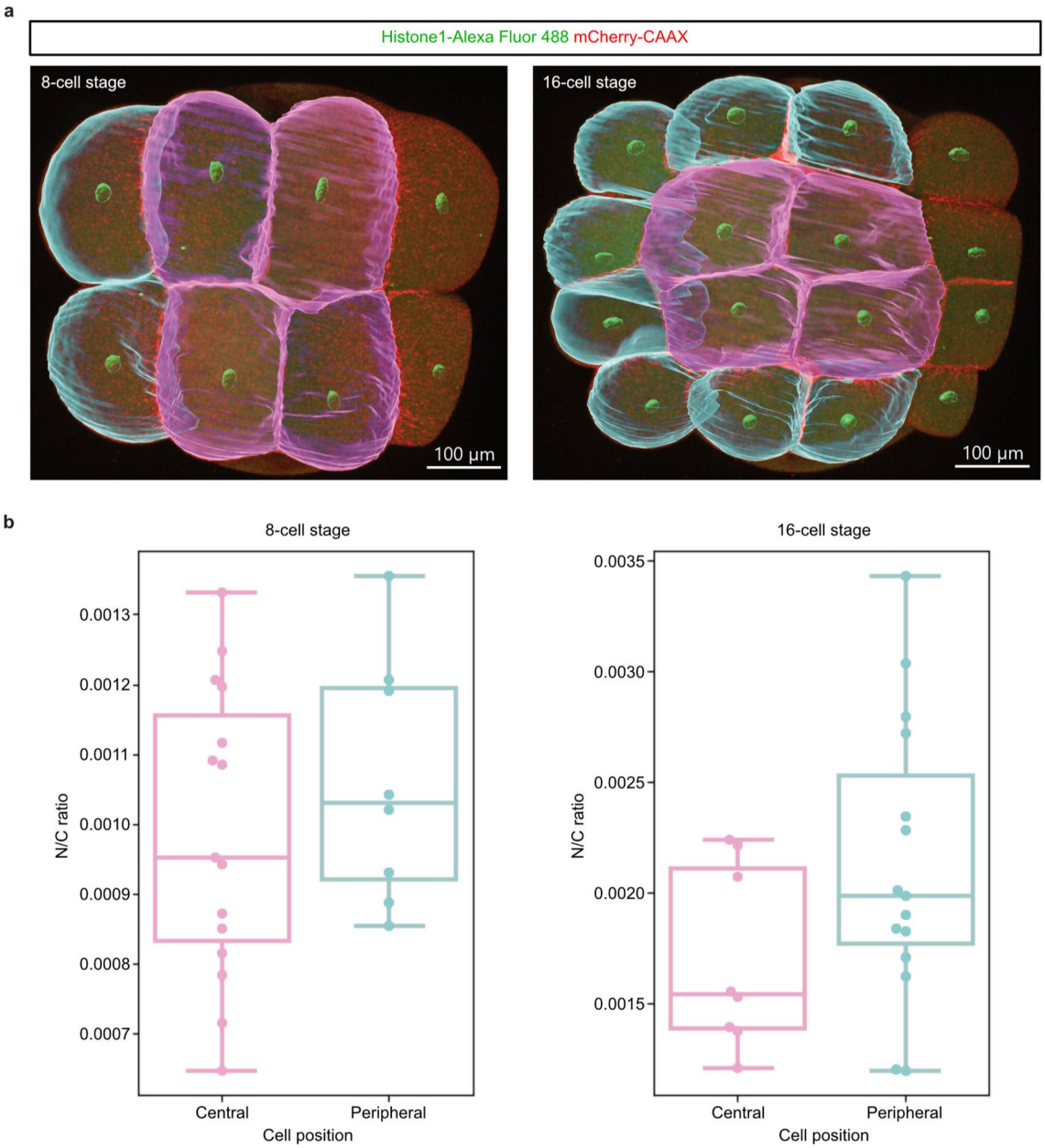

Extended Data Fig. 5 | Peripheral cells exhibit a larger N/C than central cells. (**a**) Representative images showing segmented cells and nuclei from time-lapse images of *Tg(actb2:mCherry-CAAX)* embryos injected with Histone 1-Alexa Fluor 488 at the 8- and 16-cell stages. (**b**) A dot-box plot showing the quantifications for the N/C in individual cells positioned centrally or peripherally. The boxes in the box-plots represent the middle 50% of the distribution, with the lines representing the median and the whiskers indicating the minima and maxima. n = 23 cells for each cleavage stage. Data obtained from 4 and 2 embryos for the 8- and 16-cell stage, respectively.

https://doi.org/10.1038/s41567-025-03122-1

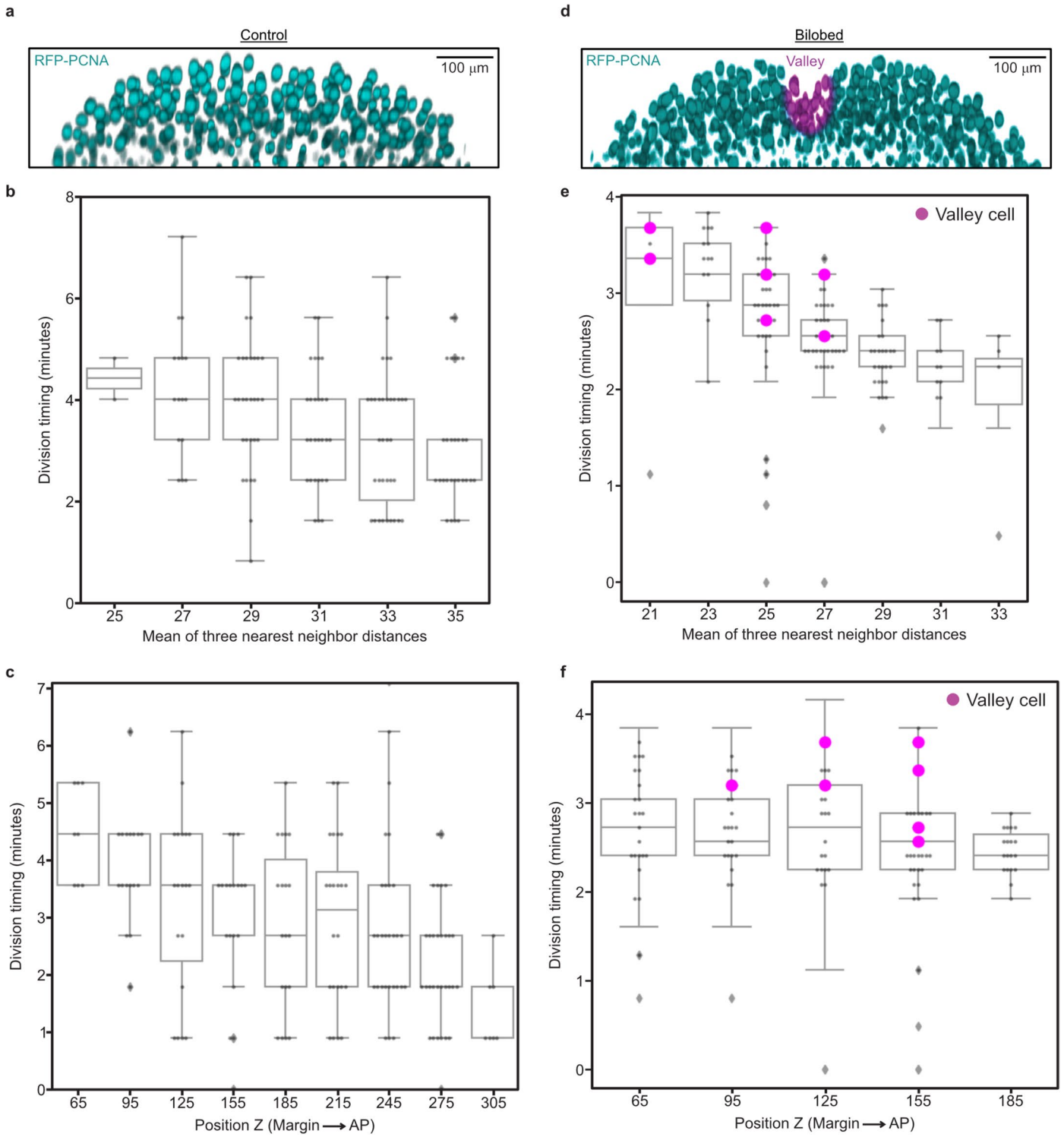

Extended Data Fig. 6 | Cell division timings correlate with cell size in bilobed embryos. (**a**, **d**) Representative lateral-view maximum intensity projections, (**b**, **e**) cell division timings as a function of the nearest neighbor distance (n = 140 and 133 cells, respectively), and (**c**, **f**) as a function of cell position along the AP-margin axis (n = 138 and 133 cells, respectively) in representative control (left) and bilobed (right) *Tg(actb2:rfp-pcna)* embryos during division round 10. The boxes in the box-plots represent the middle 50% of the distribution, with the lines representing the median and the whiskers indicating the minima and maxima. Points outside the range represent outliers. Data representative of 10 control and 5 bilobed embryos.

https://doi.org/10.1038/s41567-025-03122-1

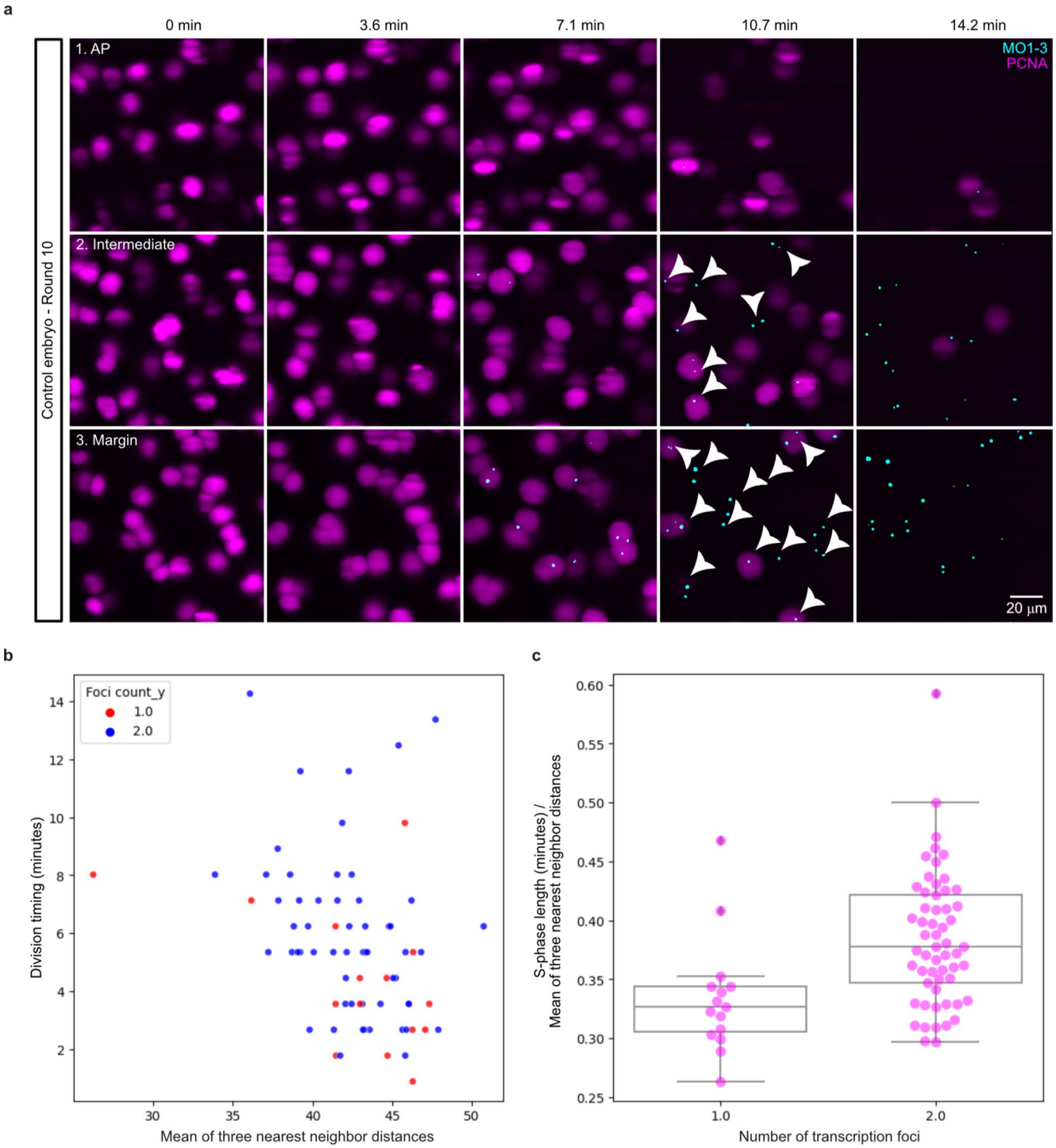

Extended Data Fig. 7 | Zygotic transcription is initiated in a patterned manner along the AP-margin axis. (**a**) Zoomed-in views of the insets (1, animal pole; 2, intermediate region; 3, margin) shown in Fig. 6A for a control Tg(*actb2:rfp-pcna)* embryo injected with MO1-3-Fluorescein in the 10th division round. Cyan, MO1-3-Fluorescein (nascent *mi430* transcripts); magenta, nuclei (PCNA). Each inset represents an area of 120 µm X 120 µm in size. (**b**) A scatter plot showing cell division timing as a function of the nearest neighbor distance with dot color representing the number of pri-mRNA transcription foci in a cell. n = 72 cells, data representative of 4 embryos. (**c**) A dot-box-plot showing the ratio of S-phase length and nearest neighbor distance for cells with one or two transcription foci for a representative embryo during division round 10. The box in the box-plot represents the middle 50% of the distribution, with the line representing the median and the whiskers indicating the minima and maxima. Dots outside the range represent outliers. n = 72 cells, data representative of 4 embryos.

nature portfolio

Corresponding author(s): Prof. Carl-Philipp Heisenberg

Last updated by author(s): Oct 23, 2025

Reporting Summary

Nature Portfolio wishes to improve the reproducibility of the work that we publish. This form provides structure for consistency and transparency in reporting. For further information on Nature Portfolio policies, see our Editorial Policies and the Editorial Policy Checklist.

Statistics

For all statistical analyses, confirm that the following items are present in the figure legend, table legend, main text, or Methods section.

n/a	Confirmed	
☐	☒	The exact sample size (*n*) for each experimental group/condition, given as a discrete number and unit of measurement
☐	☒	A statement on whether measurements were taken from distinct samples or whether the same sample was measured repeatedly
☐	☒	The statistical test(s) used AND whether they are one- or two-sided *Only common tests should be described solely by name; describe more complex techniques in the Methods section.*
☒	☐	A description of all covariates tested
☐	☒	A description of any assumptions or corrections, such as tests of normality and adjustment for multiple comparisons
☐	☒	A full description of the statistical parameters including central tendency (e.g. means) or other basic estimates (e.g. regression coefficient) AND variation (e.g. standard deviation) or associated estimates of uncertainty (e.g. confidence intervals)
☐	☒	For null hypothesis testing, the test statistic (e.g. *F*, *t*, *r*) with confidence intervals, effect sizes, degrees of freedom and *P* value noted *Give P values as exact values whenever suitable.*
☒	☐	For Bayesian analysis, information on the choice of priors and Markov chain Monte Carlo settings
☒	☐	For hierarchical and complex designs, identification of the appropriate level for tests and full reporting of outcomes
☒	☐	Estimates of effect sizes (e.g. Cohen's *d*, Pearson's *r*), indicating how they were calculated

Our web collection on statistics for biologists contains articles on many of the points above.

Software and code

Policy information about availability of computer code

Data collection	Only standard, commercial software from Zeiss (ZEN) was used for data acquisition. No custom codes were employed.
Data analysis	The use of all software (Imaris v9.9, FiJi v2.16.0/1.54p; Java 1.8.0_172, Python v3.12.9), FiJi plugins (Labkit v0.4.0, 3D Objects Counter v2.0.1, LimeSeg v0.4.2), and Python libraries (Pandas v1.5.3, Matplotlib v3.8.2, Seaborn v0.12.2) we have employed in this study have been published before, and we refer to the appropriate literature at the relevant places in the manuscript.

For manuscripts utilizing custom algorithms or software that are central to the research but not yet described in published literature, software must be made available to editors and reviewers. We strongly encourage code deposition in a community repository (e.g. GitHub). See the Nature Portfolio guidelines for submitting code & software for further information.

Data

Policy information about availability of data

All manuscripts must include a data availability statement. This statement should provide the following information, where applicable:

- Accession codes, unique identifiers, or web links for publicly available datasets
- A description of any restrictions on data availability
- For clinical datasets or third party data, please ensure that the statement adheres to our policy

Data availability: Source data have been included in the manuscript. Any additional microscopy files necessary for interpreting, verifying, and extending the research presented in the manuscript will be made available upon reasonable request to the corresponding author as they are large in size and typically require a lot of

resources to make publicly available.

Code availability: The codes used in the study are posted at: https://github.com/Irene-Li/MitoticWaves

Research involving human participants, their data, or biological material

Policy information about studies with human participants or human data. See also policy information about sex, gender (identity/presentation), and sexual orientation and race, ethnicity and racism.

Reporting on sex and gender	Not applicable
Reporting on race, ethnicity, or other socially relevant groupings	Not applicable
Population characteristics	Not applicable
Recruitment	Not applicable
Ethics oversight	Not applicable

Note that full information on the approval of the study protocol must also be provided in the manuscript.

Field-specific reporting

Please select the one below that is the best fit for your research. If you are not sure, read the appropriate sections before making your selection.

☒ Life sciences ☐ Behavioural & social sciences ☐ Ecological, evolutionary & environmental sciences

For a reference copy of the document with all sections, see nature.com/documents/nr-reporting-summary-flat.pdf

Life sciences study design

All studies must disclose on these points even when the disclosure is negative.

Sample size	All sample sizes and independent replicates are indicated in the figure legends. Experiments were typically performed on different days on embryos from different clutches. No specific tests were performed to determine the sufficiency of the sample size. However, care was exercised to examine larger sample sizes, especially in the cases where variability was high.
Data exclusions	No data were excluded.
Replication	The experiment where a nucleus is aspirated (Fig. 4) from the embryo is one that has been previously performed by Kane and Kimmel (1993). This experiment depends on the invasion of the experimental half of the embryo by nuclei from the control half. As the original authors have described, invasion does not occur in all embryos, and this point has been clarified in the main text. We analyzed only those samples where this necessary condition was fulfilled.
Randomization	Samples (embryos) were typically collected in different clutches and on different days, thereby addressing the point of random sampling.
Blinding	No blinding was performed either in data collection nor in data analysis.

Reporting for specific materials, systems and methods

We require information from authors about some types of materials, experimental systems and methods used in many studies. Here, indicate whether each material, system or method listed is relevant to your study. If you are not sure if a list item applies to your research, read the appropriate section before selecting a response.

Materials & experimental systems

n/a	Involved in the study
☒	☐ Antibodies
☒	☐ Eukaryotic cell lines
☒	☐ Palaeontology and archaeology
☐	☒ Animals and other organisms
☒	☐ Clinical data
☒	☐ Dual use research of concern
☒	☐ Plants

Methods

n/a	Involved in the study
☒	☐ ChIP-seq
☒	☐ Flow cytometry
☒	☐ MRI-based neuroimaging

Animals and other research organisms

Policy information about studies involving animals; ARRIVE guidelines recommended for reporting animal research, and Sex and Gender in Research

Laboratory animals	This work was carried out specifically with cleavage-stage zebrafish (Danio rerio) embryos, which are not considered animals at this stage as per the local regulations. All regulations were carefully followed during the research. The exact fish lines used in this study have been mentioned in the manuscript in the relevant sections.
Wild animals	Not applicable
Reporting on sex	Not applicable
Field-collected samples	Not applicable
Ethics oversight	All animal breeding and procedures were performed in accordance with the European Union animal welfare guidelines and involved only low severity lines, in accordance with the authorized animal breeding licenses (66018/8-II/3b/2013 and 2023-0.288.351) in the ISTA aquatics facility (approval no. 024-0.730.856). All experiments were performed before 5 days post-fertilization, a period during which zebrafish do not feed independently and in line with the 3R's principles.

Note that full information on the approval of the study protocol must also be provided in the manuscript.

Plants

Seed stocks	Not applicable
Novel plant genotypes	Not applicable
Authentication	Not applicable